

A rate-dependent constitutive model predicting the double yield phenomenon, self-heating and thermal softening in semi-crystalline polymers

P. Hao^{a,b,*}, V. Laheri^a, Z. Dai^{a,c} and F. A. Gilabert^a

^aGhent University (UGent), Department of Materials, Textiles and Chemical Engineering (MaTCh), Mechanics of Materials and Structures (MMS), Tech Lane Ghent Science Park - Campus A, Technologiepark Zwijnaarde 46, 9052 Zwijnaarde, Belgium

^bSIM Program M3Strength, Technologiepark Zwijnaarde 48, B-9052, Zwijnaarde, Belgium

^cTongji University, Key Laboratory of Road and Traffic Engineering of the Ministry of Education, 4800 Cao'an Road, 201804 Shanghai, P.R. China

ARTICLE INFO

Keywords:

Constitutive model
Semi-crystalline polymers
Double yield
Strain rate sensitivity
Self-heating

ABSTRACT

The double yield (DY) phenomenon observed in a wide variety of semi-crystalline polymers (SCP) adds difficulties in the material characterization. In this paper, a constitutive model, termed as explicit semi-crystalline polymer (ESCP) model, is proposed to study DY phenomenon as well as the rate- and temperature-dependent thermomechanical response below the glass transition temperature. The underlying yield kinetics due to the morphological changes of the spherulite micro-structure is represented by a rheological analogue described by a physically-based amorphous intermolecular resistance and a rate-independent crystalline interlamellar resistance. Independently-identified viscoelastic response and network resistance are also implemented to complete the model description. The activation and disclosure of the crystalline component depend on the saturated state of amorphous phase. The proposed model is validated against experimental data obtained from different authors for three commonly used SCPs: nylon 101, LDPE and PA6. A straightforward parameter identification procedure, requiring a minimum number of calibration tests, is presented to illustrate the model usage. The thermomechanical-coupled analyses provide satisfactory predictions using simulated models of a cylinder compression and dogbone tensile tests at different rates, where the self-heating and thermal softening effects are naturally captured by the model.

1. Introduction

Over the last decades, fibre-reinforced polymer composites have been widely used in multiple engineering applications thanks to their lightweight, high strength and design flexibility attributes. By using a thermoplastic (TP) polymer as matrix in these composites, the recyclability is added as an advantageous attribute. However, the usage of TP-based composites as load bearing components is still very limited due to the lack of understanding of the behaviour of the TP matrices under different temperature, moisture content and loading speed [1–6]. A semi-crystalline polymer (SCP) is a common type of thermoplastic that possesses a complex microstructure that can suffer morphological changes hindering enormously its thermomechanical characterization [7–9]. SCPs are typically formed by the packing of spherulites in which the amorphous phase and the crystalline lamellar nanoblocks are randomly distributed [10, 11]. The interaction between the amorphous and the crystalline phases at both micro- and nano-scales can lead to significantly different yield kinetics compared to purely amorphous polymers. This interaction is sensitive to temperature as well as to the rhythm of deformation and it can generate a double yield point remarkably visible in macroscopic stress-strain curves.

The double yield (DY) phenomenon has been reported for polyamide (PA) [3, 12–17], polytrimethyleneterephthalate (PTT), polybutyleneterephthalate (PBT) [18] and polyethylene (PE) [19–22]. Fig. 1 presents a typical stress-strain curves for nylon 101 with two clear yield points [12]. The first yield point ($\sigma_{y,1}$) is located at a strain around 5%. Researchers have proposed that $\sigma_{y,1}$ is related to the amorphous phase [10, 12, 20]. Parodi [16] studied the yield stress verifying whether the internal resulting plastic strain rate equals the applied strain rate. Rozanski and

*Corresponding author

✉ pe.i.hao@ugent.be (P. Hao)
ORCID(s): 0000-0002-8620-026X (P. Hao)

Galeski [23] examined the first yield in SCPs by modifying the swelling in the amorphous phase and they confirmed that plastic yielding of this phase was greatly affected and a stress reduction of the yield point was observed. Krajenta and Rozanski [24] also investigated the effect of the physical state of the amorphous phase on the thermo-mechanical properties of polypropylene (PP) introducing modifiers into the amorphous phase regions. The second yield point ($\sigma_{y,II}$) at the strain around 30% can be explained by the crystallographic slip mechanisms of the intra-crystalline nanoblocks or shear bands formation in the inter-crystalline domains. Bartczak and Galeski [25] studied the plastic deformation process and the crystallographic slip mechanisms (fine chain slip, coarse chain slip and interlamellar shear) under tension and compression. They pointed out that both amorphous and crystalline phases are strongly connected, leading to a simultaneous and consistent deformation of both phases. Also, the crystalline phase is highly affected by the partially reversible shear deformation of amorphous layers. The shear on the crystalline blocks and the influence on the yield mechanisms of PE were analysed by Plaza *et al.* [26]. As SCPs is monotonically deformed, the morphological changes accompanied with the rearrangement of the spherulitic structure into the form of parallel microfibrils occurs till the final rupture [20, 25, 27]. G'sell and Dahoun [28] have investigated the microstructural transformations induced by the deformation for PE and polyetheretherketone (PEEK) with certain crystallinity degrees. The underlying DY phenomenon can be clearly observed within a SCP with a specific diameter of spherulite [11] and under certain conditions, for instance, high strain rate, low temperature [29] or low moisture content [15]. Also, Luo *et al.* [13] studied the effect of water and thermal treatment on the DY phenomenon of PA6 blends and neat PA6 in tension. Nitta and Kuriyagawa [30] studied DY phenomenon of a metallocene-catalyzed HDPE in tension using catastrophe theory. The initiation and propagation of necking were explained by the microstructure rearrangement of locally-formed cluster units of the single chain. To prevent any nonlinear geometrical effect (e.g., necking) on the appearance of the second yield point under tensile tests, cylindrical samples in compression are generally recommended [19]. To study the yield loci of SCPs, Farrokh and Khan [31] developed an empirical pressure- and rate-dependent initial yield criterion for a macroscopically isotropic SCP nylon 101. Hachour *et al.* [32] proposed a micromechanics-based two-phase criterion for yielding of SCPs considering the effects of different crystallinities. Polińska *et al.* [33] recently proposed a method to determine the modulus of interlamellar amorphous phase of SCP with an illustration of HDPE. They observed that there exists a linear increase in the modulus of interlamellar amorphous phase with the increase of crystallinities thanks to the decrease in "deformability" of the amorphous phase.

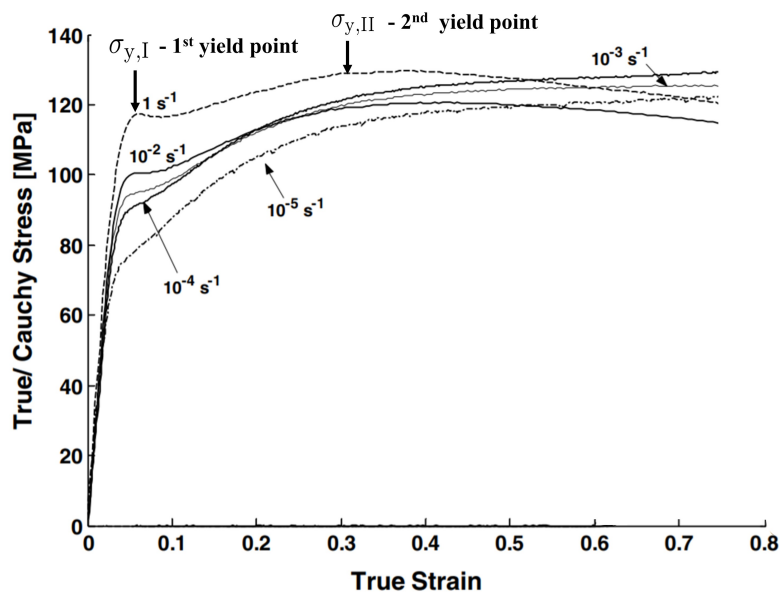


Figure 1: True stress-strain curves in nylon 101 under uniaxial compression exhibiting the DY phenomenon (Adapted from Ref. [12]).

Constitutive models for SCPs have been developed either via phenomenological or physically-based approaches focusing on the large deformation of polymers, where macroscopic pre- and post- yield were studied. A phenomenological approach usually adopts a function to mathematically describe the flow stress in terms of both temperature and

strain rate. Generally, the behaviour of amorphous and crystalline phases are considered explicitly. With microstructural considerations, Lai *et al.* [34] formulated a nonlinear viscoelastic model for SCP under small strain and isothermal conditions, where a perfectly elastic response of crystalline phase was assumed. Ayoub *et al.* [35] modelled the contribution of amorphous and crystalline phases acting in parallel to study the large deformation behaviour of HDPE at room temperature by adopting the viscoplasticity theory based on overstress (VBO) [36–38]. Khan *et al.* [39] characterized and modelled ultra high molecular weight polyethylene (UHMWPE) using the modified VBO. The modified model was developed to capture the rate-reversal behaviour in creep and relaxation due to the loading history. Alternatively, Drozdov and Christiansen [40] assumed the SCP as an effective isotropic homogeneous medium instead of formulating a physical model including all possible micromechanisms. Similarly, Khan and Zhang [41] combined a viscoelastic standard solid model with a viscoplastic component to describe polytetrafluoroethylene (PTFE) under quasi-static and dynamic loads. Balieu *et al.* [42] formulated a new phenomenological elasto-viscoplastic damage model with pressure-dependent yield surface for mineral filled PP and validated with uniaxial tension and compression tests. Balieu *et al.* [43] also proposed a damage characterization method for SCPs under high strain rates using digital image correlation (DIC). This method was compared to the classical damage characterization by the loss of stiffness and it proved suitable for measuring ductile damage. Readers are referred to these approaches without considering micromechanisms [4, 5, 44–46].

On the other hand, a physically-based approach generally considers the material macromolecular structure with some idealized assumptions. Therefore, the identified material parameters possess physical meanings. These approaches can be divided into micromechanical, two-phase analogue and effective amorphous ones:

Micromechanical approach is inspired by composite inclusions to construct multiscale models where the internal structure is explicitly described. A pioneer model was proposed by Lee *et al.* [47, 48], where the amorphous layers and crystalline lamellae were idealized by a plate-like structure. This model made it possible to study the texture evolution of HDPE under different loadings. Similarly, Nikolov *et al.* [49, 50] proposed a multiscale model with high crystallinity degree and it was validated with HDPE within a temperature range above the glass transition temperature at small strains. Their results confirmed that shear in the amorphous phase is the dominant deformation mechanism under small strains. Inspired by the elasto-viscoplastic inclusion model developed by van Dommelen *et al.* [51], Sedighiamiri *et al.* [20] studied the DY phenomenon observed for uniaxial compression data of HDPE. Several micromechanical models have been compared in terms of Young's modulus vs. crystallinity by Bedoui *et al.* [52] for three widely used SCPs: PP, PE and polyethyleneterephthalate (PET). Shojaei and Li [53] formulated a new viscoplastic constitutive law for the glassy amorphous phase of SCP provided with pragmatical calibration procedure. The multiscale approach and the new viscoplastic model combining with the crystal plasticity were validated for polymeric material systems considering the morphological texture changes. Uchida and Tada [54] developed a micro-, meso- to macroscopic computational model using FE-based homogenization method to investigate HDPE. Voyiadjis *et al.* [55] characterized the microscale mechanical response of glassy SCP for microstructural applications using a rate-dependent plasticity theory with strain gradient effects, where kink mechanisms of molecular chains in crystalline polymers were studied using non-local gradient plasticity approach from metals.

Two-phase analogue approach considers the contribution of amorphous and crystalline phases regardless of the interaction between both phases. Ahzi *et al.* [56] proposed a model by adopting the same physically-based glassy amorphous model in both the crystalline and the amorphous phases, following the intermolecular resistance modified by Boyce *et al.* [57]. Based on this work, Makradi *et al.* [58] proposed a constitutive model for large deformation behaviour of PET above the glass transition temperature. Ayoub *et al.* [59] also proposed a modified version based on these prior works to study PE under large deformation with a broad range of crystallinities. Abdul-Hameed *et al.* [60] revised and extended the two-phase model applying for the PE-based materials to describe the influence of different crystallinities. In their approach, the macroscopical hyperelastic–viscoplastic response corresponding to the network and intermolecular resistances considers the coupling of crystalline and amorphous phases. This new extension combining with a parameter optimization fitting procedure reproduced good results for HDPE, LDPE and ULDPE. Cayzac *et al.* [61] proposed a multi-mechanism (MM) constitutive model incorporating damage and crystallinity to investigate PA6. Popa *et al.* [62] used a homogenization approach with a representative mesostructure of a convex polyhedron element and the micromechanics to describe amorphous and crystalline phases. They introduced a new phenomenological evolution law for the athermal shear strength in the constitutive model used for the amorphous and which is combined with an elastoplastic microscopic crystalline model. The model was validated with isotactic polypropylene (iPP) under quasi-static and dynamic loads. Recently, Ayoub *et al.* [63] developed a physically-based approach to model the mechanical and fracture response of LDPE with ageing effect through the acceleration of

ultraviolet radiation (UV). The UV ageing effect was incorporated by the alteration of the molecular weight, which updates the evolution of the crystal content, network and intermolecular resistances.

Effective amorphous approach is used when the amorphous phase dominates the global mechanical response of SCPs. Maurel-Pantel *et al.* [64] extended the visco-hyperelastic constitutive model developed by Billon [65] to a three-dimensional constitutive formalism within a thermodynamic framework for PA66. Garcia-Gonzalez *et al.* [2] proposed a hyperelastic-thermoviscoplastic constitutive model for a high performance thermoplastic PEEK at different strain rates using thermomechanical-coupled (TMC) analyses.

To cover a wide strain rate range, it is essential to conduct a TMC analysis to account for the self-heating and thermal softening effects observed at elevated strain rates [66]. Anand *et al.* [67] developed an amorphous model with TMC theory accounting for the large deformation and Ames *et al.* [68] applied this theory to capture the intrinsic rate- and temperature-dependent features as well as the self-heating effect on the temperature rise using FEM. Jena *et al.* [69] further apply the TMC constitutive model developed by Srivastava *et al.* [1] to simulate the fabrication of microfluidic devices using cyclic olefin copolymers (COCs) in a wide temperature range. This numerical simulation-based design enables to estimate appropriate processing parameters instead of classical trial-and-error techniques. Bouvard *et al.* [70] developed a fully TMC model for the glassy amorphous polymer using physically-based internal state variables considering the entanglement points and material hardening. Amorphous polycarbonate (PC) was validated with the rate-, temperature- and stress state-dependent constitutive model under different loading conditions. The temperature rise due to the plastic dissipation at an elevated strain rate was captured. A predictive model covering in a natural way a wide range of thermomechanical responses (e.g., from isothermal to nearly adiabatic) is still needed, and only few models can partially be used under non-isothermal conditions [2, 4–6, 71–73].

To authors' best knowledge, the DY phenomenon can only be captured by few micromechanical models [20, 54]. However, there is a lack of constitutive models enabling to quantitatively predict the DY phenomenon for different types of SCPs. In this paper, we proposed a different approach to capture the DY phenomenon considering different deformation regimes of the amorphous and crystalline phases. This approach is practical and efficient, particularly suitable for engineering applications.

In this work, a double yield model, termed as explicit semi-crystalline polymer (ESCP) model, is proposed below the glass transition temperature. This paper is organized as follows. Section 2 and 3 present an overview of the thermomechanical behaviour of general thermoplastics and the double yield kinetics in SCPs. Section 4 presents a double yield constitutive model and it is illustrated with the microstructural morphological transformations. The finite strain kinematic framework and the constitutive model are presented in Section 5. Section 6 presents the dissipation and the heat balance equation. The details of the numerical implementation are documented in Section 7. Section 8 presents the validation procedure of the model for nylon 101, LDPE and PA6 covering the full range of thermomechanical scenarios. The parameter identification procedure and sensitivity analyses are provided in Appendices.

2. Overview of the thermomechanical response of thermoplastics

The mechanical response of thermoplastic polymers has been widely investigated under different testing conditions, and the experimental results show that they highly depend on loading type, loading speed, temperature, relative humidity, or ageing, among others. Some of these effects are summarized as follows:

- Rate dependency: thermoplastics exhibit a viscoelastic and viscoplastic response as Fig. 2 shows. This rate-sensitivity is resulted from the molecular bases of relaxations. Particularly, it leads to produce an increase of the young modulus and peak yield stress when the applied strain rate is increased [29, 74].
- Pressure sensitivity and tension-compression asymmetry: higher stress levels can be observed in compression compared to tension due to the effect of hydrostatic pressure. Meanwhile, a sudden drop is commonly observed in tension due to the necking effect induced by geometrical nonlinearities in the specimen. Therefore, true stress-strain curves are always recommended to characterize the intrinsic material behaviour. Besides, a compressive test is recommended to minimize the effect of micro voids and crazing [19].
- Thermal softening and self-heating: the stiffness and strength of thermoplastics are very sensitive to temperature. In general, an increase of temperature can reduce drastically all the mechanical properties [2, 66]. Also, under high strain rate, self-heating takes place, which is caused by the dissipated plastic energy that can not be released sufficiently fast to the environment but it is internally retained. Fig. 1 shows that these effects can raise temperature, leading to a clear thermal softening (for $\dot{\epsilon} = 1 \text{ s}^{-1}$).

- **Relative humidity:** an increase of relative humidity produces a similar effect as the increase of temperature. This was recently investigated in PA6 under uniaxial tension [3]. This research proves that the humidity can be treated as an "apparent temperature" when a Ree-Eyring behaviour is assumed to govern the plastic deformation.

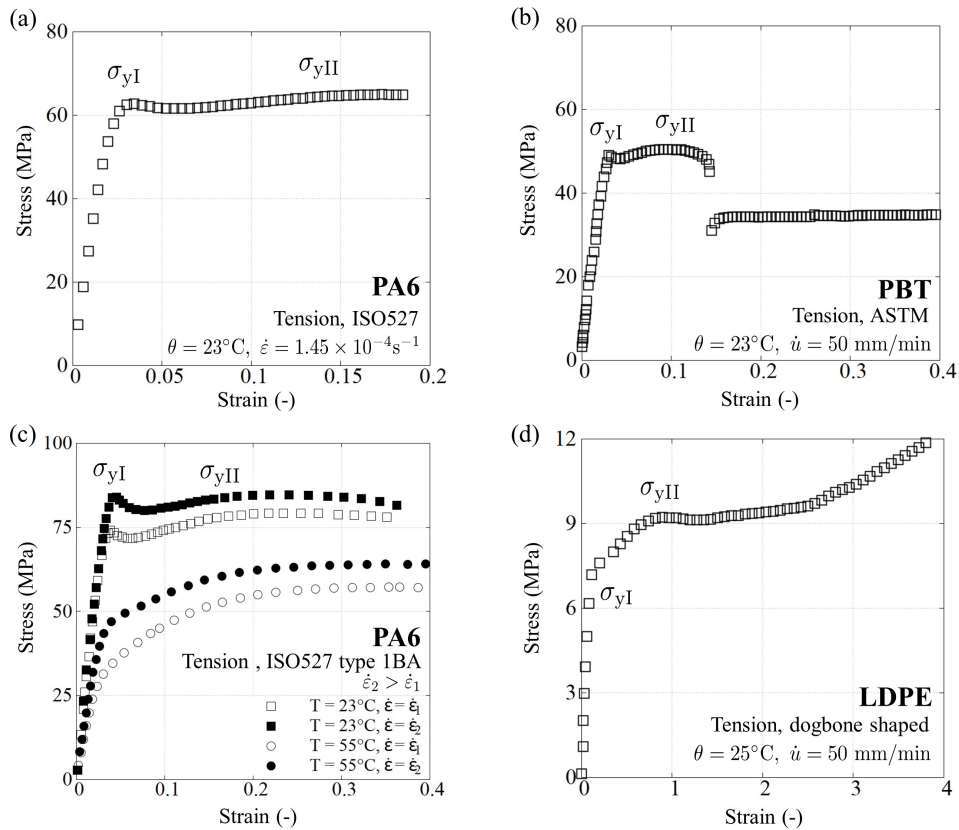


Figure 2: Experimental stress-strain curves of different semi-crystalline polymers (PA6 [3], PBT [18], and LDPE [21]) exhibiting DY phenomenon and measured using different standards.

3. Physics of deformation of semi-crystalline polymers

3.1. Double yield phenomenon

A SCP contains spherulites with crystalline lamellae embedded in the amorphous media. Apart from the features described before, the interaction between the crystalline and amorphous phases complicates the understanding of the evolution of the mechanical response, from which, a double yield point emerges. The DY phenomenon has been reported for different SCPs regardless of the stress and strain measures adopted by other authors (Fig. 2) and it is more prominent when several conditions are met: at relative low moisture level, low temperature and high strain rate. These conditions inherently have influence on the mobility of the polymer chains altering the intermolecular resistance. For instance, in PA the DY is typically not observed from stress-strain curves when the relative humidity is 50% [5, 14, 15]. However, DY occurs inherently due to the interaction of two phases in the microstructure. The first yield may be hidden under certain testing conditions or simply being very subtle in some materials. For example, no remarkable "hump" can be observed when the relative humidity is unintentionally included.

A commonly used definition of yield point in polymers relies on checking whether the internal plastic flow rate equals the applied strain rate, what it leads to a local maximum in the stress-strain curves [16]. However, this definition is not sufficient for SCPs with a double yield point. By increasing the temperature, the first yield becomes less pronounced and the sharp transition disappears (see the σ_{yI} at 55°C in Fig. 2(c)). Some polymers experience total elastic recovery after unloading beyond this yield point. However, other SCPs experience clear permanent plastic

deformation even prior to this point. Brooks *et al.* [19] proposed an alternative definition of yield for PE and residual strain experiments, confirming the existence of two yield points. The DY was correlated to the gradient changes in residual strain-applied strain curves. The results suggested that both points are connected to the details of the evolution of the internal blended microstructure, where amorphous and crystalline phases can interact at different strain levels [29].

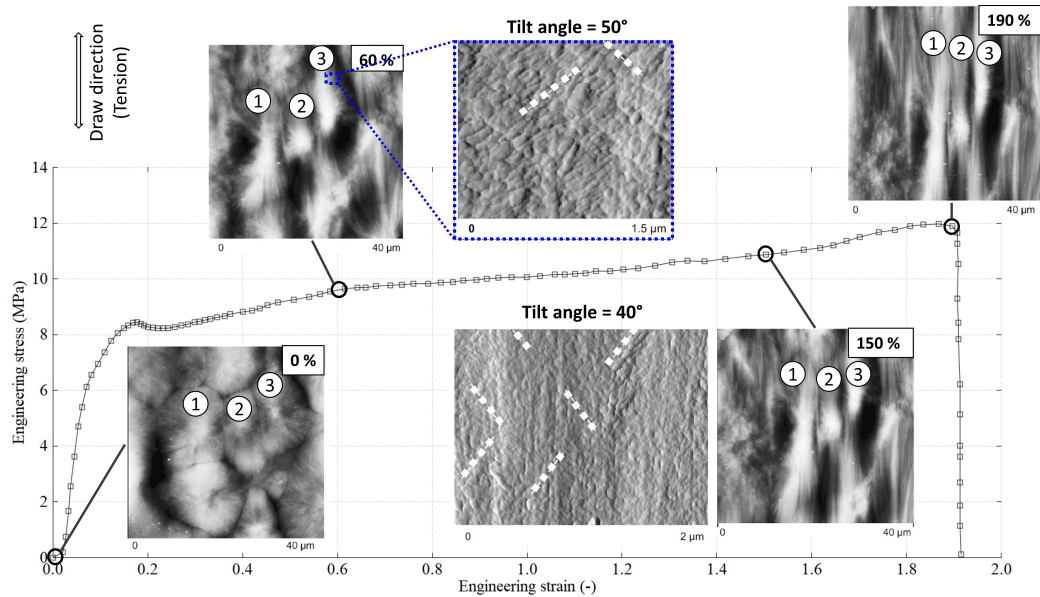


Figure 3: In-situ AFM study of polybutene under tensile drawing where white dotted lines indicate the alignment of the crystal fragments from 50° to 40° along the tensile direction (Adapted from Ref. [11]).

3.2. Double yield kinetics

The investigation on the texture evolution performed by Sedighiamiri *et al.* [20] confirms that the DY phenomenon arises from clear morphological changes of the internal structure. **The first yield point** typically takes place at low strain ($\epsilon \lesssim 5\%$) and it is mainly originated in the amorphous phase [12, 20]. Above the glass transition temperature (θ_g) and below melt temperature (θ_m), the first yield vanishes from the stress-strain curve [29] whereas the crystalline phase remain unaffected. The thermally-activated mechanism of yielding in amorphous polymer was described by Argon [75] using the physically-based concept of the double kink production process, where movement of the molecular segments is connected to the irreversible deformation. **The second yield point** is attributed to the crystalline phase and it takes place at higher strain levels ($\epsilon \gtrsim 10\%$). It was proved by comparing two different grades of PA6 with different crystallinity degrees. The second yield is less pronounced for the one with lower crystallinity degree [29].

In order to capture the DY phenomenon in the mechanical modelling, the deformation processes at the different scale levels of the structure should be understood. The plastic deformation in SCPs under tensile drawing has been studied at micro- and nano-scales using Atomic Force Microscopy (AFM) [10, 11]. Fig. 3 shows that polybutene (PB) film with an average spherulite diameter of 20 μm presents two clear yield points at room temperature at strain rate of 10^{-3} s^{-1} [11]. The in-situ images from AFM do not show fibrillar transformation during the loading period. Instead, all spherulites deformed elliptically up to the rupture, showing a decrease of the tilt angle between the crystal fragments and the draw direction from 50° to 40° when the applied strain increases from 60% to 150%. Donnay *et al.* [76] conducted the in-situ study of the micro-mechanism of PET under tensile drawing using X-ray scattering. The macromolecular orientation in both amorphous and crystalline phases was clearly examined and the tilted lamellae along the tensile axis was also observed. This indicates a rotation of internal crystal fragments accompanied by a continuous yielding of the amorphous region. Postmortem AFM observations on PA6 film showed that shear bands nucleate and propagate in the amorphous phase [10], where the second yield was not reported as no crystal slip happened at the investigated strain range. Nevertheless, these AFM-based tests were conducted using ultra-fine polymer films, therefore, the effects of the thickness on crystal slip could not be discussed. In spite of the

experimental difficulties to obtain clear images inside of the crystal lamellae, other key mechanisms like damage (crazing and cavitation) or microfibrillar transformation, have been discussed by other authors [7, 9, 27].

4. Proposed material model

4.1. Description of double yield model

According to the yield kinetics in SCPs, we propose a modular physically-based viscoelastic-viscoplastic double yield model to quantitatively predict the full thermomechanical response of SCP with double yield point. Rate-sensitivity, thermal softening and self-heating are also covered at a wide range of strain rates. This model is flexible to characterize different thermoset and thermoplastic polymers. Fig. 4 schematically represents the proposed double yield model at two types representative strain rates, considering the experimental observations shown in Fig. 2. In order to quantitatively incorporate a rate- and temperature-dependent thermomechanical response, we divide the mechanical response in six stages:

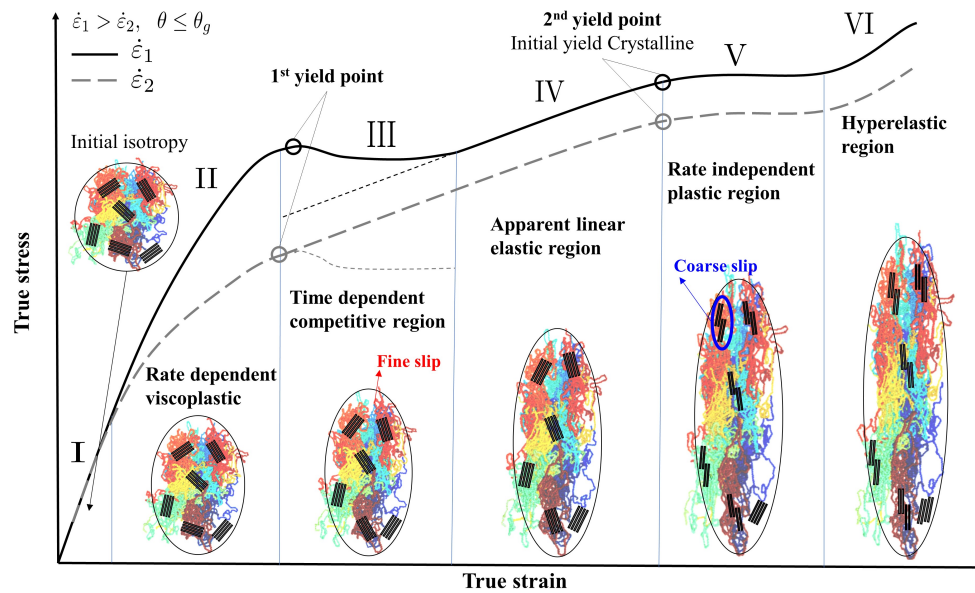


Figure 4: Schematic description of true stress-strain response in semi-crystalline polymers at different strain rates and the corresponding morphological changes.

- (I) (Visco)elasticity: Both the amorphous and crystalline phases deform elastically. A more pronounced nonlinear viscoelastic response is observed at higher temperatures. The deformation is still reversible when the specimen is unloaded.
- (II) Viscoplasticity: The plastic strain rate in amorphous phase evolves to catch up the applied strain rate (i.e. fine slip). At the end of this stage, a homogeneous plastic deformation takes place, leading to the occurrence of first yield in amorphous phase without any crystal slips (i.e. coarse slip).
- (III) Shear bands formation: The morphological changes lead to the formation of shear bands and crystalline lamellar blocks. The crystalline blocks deform elastically and rotate along the elliptical transformation of spherulites. The amorphous phase experiences strain softening before reaching a saturated state. The competition between the crystalline and the amorphous phases results in a sharp or smooth transition at high or low strain rates, respectively.
- (IV) Apparent secondary linear elastic regime: The amorphous phase reaches the saturated state (i.e. constant stress level) whilst the crystalline phase continuously deforms elastically. The increase of the total stress is contributed by the crystalline phase. Fig. 3 shows the alignment of the crystal fragments with rigid rotation, providing the evidence of linear elastic response in the crystalline phase.

- (V) Rate-independent plasticity: The second yield appears due to the crystal slips (coarse slips). It becomes the dominant mode of plastic deformation, resulting in crystalline lamellar fragmentation at the second yield. Fig. 2(c) shows the stress-strain curves with a parallel trend after second yield point regardless of the applied strain rate.
- (VI) Hyperelasticity: Network resistance due to polymer chain reorientation at large deformation, which is related to the molecular alignment and micro-fibrillar transformation before failure (see Fig. 2(d)).

4.2. Rheological representation

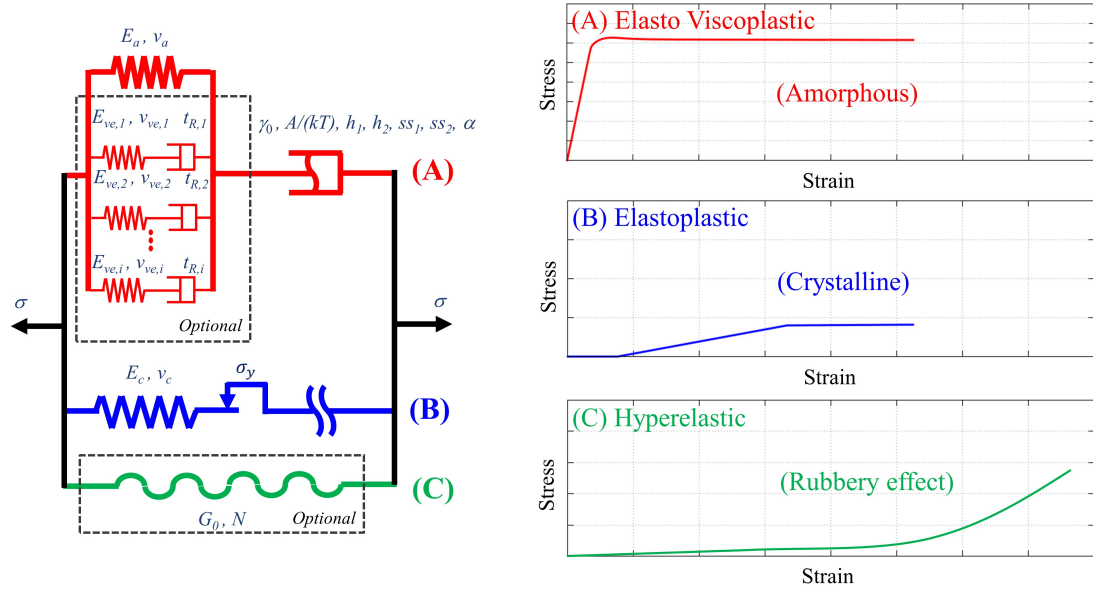


Figure 5: Rheological analogue of the proposed constitutive model and the contribution of the three main components.

One of the most widely used rheological model was proposed by Haward *et al.* [77]. This model suggests that there exists two physically distinct resistances under large deformation: (i) the intermolecular resistance that has to be overcome to initiate the yield and (ii) the network resistance related to the configurational entropy due to polymer chain reorientation. Following this scheme, Fig. 5 shows the rheological model consisting of three components: (A) an intermolecular resistance accounting for the fine slip, (B) a crystalline interlamellar resistance representing the coarse slip, and (C) a network resistance representing the rubbery effect. According to the experimental observations, the component accounting for the crystalline contribution is assumed to be rate- and temperature-independent. When the first yield in amorphous is achieved, the activation of the crystalline component is controlled by an embedded "switch" (see Fig. 5). A rate-dependent characteristic time t_c is introduced to emulate the results from the interaction between both phases. The stress contribution of the crystalline component before the first yield is assumed to be zero and the total elastic behaviour is governed by the amorphous phase. There are two reasons for this hypothesis: (1) the AFM observations of the rigid rotation of the crystalline phase, and (2) the strain-softening followed by crystalline contribution is capable to be captured with a "hump" (remarkable DY) at a high strain rate. It can be easily identified and quantified from experimental curves under standard testing conditions.

The proposed model is aimed at being practical, efficient and easy to implement. The material characterization is straightforward, requiring a small number of tests. The optional features (viscoelastic and hyperelastic response) can be identified by performing additional calibration tests separately. This model reduces to the glassy amorphous model if the crystalline module is ignored, which was also used to characterize thermoset polymers [74].

5. Mathematical model formulation

Following the finite strain kinematic framework, the nonlinear behaviour of SCP is modelled in rate form gathering several material features: viscoelasticity, viscoplasticity, elastoplasticity and hyperelasticity [78]. The breakdown of

the overall deformation resistance is represented by the schematic analogue into three resistances. An amorphous intermolecular resistance (resistance A) cooperating with a crystalline interlamellar resistance (resistance B) and a network resistance (resistance C) are depicted in Fig. 5. These three resistances acting in parallel lead to the same deformation gradient equating to the imposed deformation gradient F as

$$F_{\pi} = F, \quad (1)$$

where the subscript " π " can be "A", "B", or "C" to represent the amorphous, crystalline and network resistances, respectively. Following this decomposition, the total Cauchy stress is straightforwardly given by

$$\sigma = \sigma_A + \sigma_B + \sigma_C. \quad (2)$$

5.1. Resistance A: intermolecular resistance of amorphous phase

The viscoelastic and viscoplastic responses are coupled in this resistance by connecting in series a viscoplastic dashpot and a Prony series. The imposed deformation gradient F_A can be decomposed multiplicatively into two components as follows

$$F_A = F_A^e F_A^p, \quad (3)$$

where F_A^e is deformation gradient portion imposed on the linear spring and F_A^p the one for the dashpot. Note that Maxwell branches act in parallel with the linear spring, the deformation gradient $F_A^{ve,i}$ on the i^{th} Maxwell branch, therefore, equals to F_A^e . The inelastic deformation gradient F_A^p has to be determined to calculate the elastic deformation gradient by $F_A^e = F_A F_A^p^{-1}$. The inelastic deformation gradient F_A^p can be updated by considering the corresponding rate kinematics. The velocity gradient L_A of branch A is written as

$$L_A = \dot{F}_A F_A^{-1} = L_A^e + L_A^p = L_A^e + F_A^e L_A^p (F_A^e)^{-1}, \quad (4)$$

where L_A^p is the plastic velocity gradient expressed in the relaxed configuration, described by the rate of the inelastic contribution and it can be split into symmetric and skew parts, namely the inelastic rate of deformation D_A^p and the inelastic spin tensor W_A^p :

$$L_A^p = \dot{F}_A^p F_A^p^{-1} = D_A^p + W_A^p \quad (5)$$

The amorphous phase is isotropic, leading to a spin-free plastic velocity gradient $W_A^p = 0$ (see Ref. [79]). In this case,

$$\dot{F}_A^p = D_A^p F_A^p \quad (6)$$

The Cauchy stress tensor in resistance A is calculated in terms of the elastic deformation gradient F_A^e as follows

$$\sigma_A = \frac{1}{\det [F_A^e]} (\lambda_A \text{tr}[\mathbf{h}_A] \mathbf{I} + 2\mu_A \mathbf{h}_A) + \sum_{i=1}^{N_{ve}} \sigma_A^{ve,i}, \quad (7)$$

where λ_A and μ_A are the Lamé parameters, \mathbf{I} the identity tensor, $\mathbf{h}_A = \ln(\sqrt{\mathbf{B}_A^e})$ the Hencky strain with the elastic Cauchy-Green tensor $\mathbf{B}_A^e = \mathbf{F}_A^e \mathbf{F}_A^{eT}$ and N_{ve} is the number of viscoelastic Maxwell branches. The calculation of the stress contributions of the Maxwell branch $\sigma_A^{ve,i}$ is presented in Appendix C. According to the experimental observation of nylon 101, LDPE and PA6, the viscoelastic response is not included in the model validation in the present work.

However, for the sake of completeness of the model, the full model is developed and the effect of the viscoelasticity is explored with assumed parameters (refer to Appendix C).

Among a wide diversity of glassy polymer models, there are three important ones: macromolecular Boyce-Parks-Argon (BPA) model [57, 66, 80], Eindhoven Glassy Polymer (EGP) model [81–83] and Oxford Glass Rubber (OGR) model [84]. Despite of their underlying physical interpretation, these models are equivalent in terms of fitting procedure for the parameter identification. This research follows a physically-based glassy amorphous polymer model based on BPA model to describe the viscoplastic response capturing the first yield [85]. The softening and hardening evolution follow the phenomenological equation postulated in Ref. [74, 85].

The explicit solution of the rate of plastic deformation in terms of an effective plastic strain rate $\dot{\bar{\epsilon}}_A$ and direction tensor \mathbf{N} are given as follows

$$\mathbf{D}_A^p = \dot{\bar{\epsilon}}_A \mathbf{N}, \quad \mathbf{N} = \frac{3}{2\sigma_{\text{eq}}} \boldsymbol{\sigma}'_A, \quad (8)$$

where the driving stress $\boldsymbol{\sigma}'_A$ is the deviatoric part of $\boldsymbol{\sigma}_A$ and the equivalent stress σ_{eq} is defined by

$$\sigma_{\text{eq}} = \sqrt{\frac{3}{2} \boldsymbol{\sigma}'_A : \boldsymbol{\sigma}'_A}. \quad (9)$$

The effective plastic strain rate $\dot{\bar{\epsilon}}_A$ was explicitly prescribed by modifying the expression in terms of the plastic strain rate originally derived by Argon [75] for the free energy barrier to release the polymer chain double kinks in amorphous polymer, which is given as follows

$$\dot{\bar{\epsilon}}_A = \dot{\epsilon}_0 \exp \left[-\frac{A (s - \alpha_p \sigma_h)}{\theta} \left(1 - \left(\frac{\sigma_{\text{eq}}}{s - \alpha_p \sigma_h} \right)^m \right) \right], \quad (10)$$

where α_p is the pressure sensitivity parameter leading to tension and compression symmetry, θ the absolute temperature and σ_h hydrostatic part of Cauchy stress tensor. The constants $\dot{\epsilon}_0$, A and m are the rate-dependent sensitivity parameters that should be identified from the peak yield stresses at different strain rates. The so-called athermal effective stress s is related to the temperature-dependent shear modulus, where its initial value s_0 is given by

$$\frac{s_0}{\mu(\theta)} = \sqrt{3} \frac{8.5^{-1/m}}{(1 - \nu)}, \quad \mu(\theta) = \frac{E(\theta)}{2(1 + \nu)}, \quad \log \frac{E_{\text{ref}}}{E(\theta)} = \beta (\theta - \theta_{\text{ref}}). \quad (11)$$

The identification of the parameter β requires the experimental measurements of the elastic modulus $E(\theta)$ at different temperatures. For the studied cases, the reference temperature was chosen as room temperature (22°C for nylon 101 and LDPE, and 23°C for PA6). To capture the post-yield strain softening, the evolution of \dot{s} has been modified by incorporating the pressure sensitivity in a phenomenological softening equation [80]. Later, this strain softening equation was heuristically modified to consider the pre-yield nonlinearity, leading to a redefinition of yield as peak yielding point. This approach has been validated for Epoxy Epon 862 [74]. The starting point of this pre-peak nonlinearity was chosen as a stress level at strain of 0.01. The time derivative of the athermal effective stress is built upon a heaviside function to mirror the post-yield strain softening to pre-yield nonlinear curvature with a different hardening parameter h_1 . This form relates the athermal shear stress s_0 at the pre-defined initial yield stress to s_1 at the peak yield stress while remaining the strain softening from s_1 to the saturated state s_2 (low yield), and it is expressed as

$$\dot{s} = H_1(\bar{\epsilon}) \left(1 - \frac{s}{s_1} \right) \dot{\bar{\epsilon}}_A + H_2(\bar{\epsilon}) \left(1 - \frac{s}{s_2} \right) \dot{\bar{\epsilon}}_A, \quad (12)$$

where the smooth functions $H(\bar{\epsilon})$ are given by

$$H_1(\bar{\epsilon}) = -h_1 \left\{ \tanh \left(\frac{\bar{\epsilon} - \bar{\epsilon}_p}{f \bar{\epsilon}_p} \right) - 1 \right\}; \quad H_2(\bar{\epsilon}) = h_2 \left\{ \tanh \left(\frac{\bar{\epsilon} - \bar{\epsilon}_p}{f \bar{\epsilon}_p} \right) + 1 \right\}, \quad (13)$$

where h_1 and h_2 are the hardening (softening) parameters, f the smoothing factor and $\bar{\epsilon}_p$ the plastic strain at the peak yielding point.

The main reason of choosing this BPA-based model is due to the nonlinearity in the pre-yield ($\sigma_{y,I}$) stage observed in semi-crystalline polymers under tension and compression, where this pre-peak nonlinear behaviour is correctly represented.

5.2. Resistance B: interlamellar resistance of crystalline phase

For nylon 101 [12], LDPE [22] and PA6 [29] investigated in this paper, a saturated state is established when the local low stress level is observed following the strain softening after the first yield point. Then, the shape of stress-strain curves follows the same trend regardless of the applied strain rates, implying that an elastoplastic constitutive model is suitable to characterize this rate-independent response. The same decomposition scheme of deformation gradient is applied for the interlamellar resistance of crystalline phase.

$$\mathbf{F}_B = \mathbf{F}_B^e \mathbf{F}_B^p \quad (14)$$

The Hencky strain $\mathbf{h}_B = \ln(\sqrt{\mathbf{B}_B^e})$ is calculated with the elastic Cauchy-Green tensor $\mathbf{B}_B^e = \mathbf{F}_B^e \mathbf{F}_B^{eT}$. A pressure-dependent elastoplastic model based on paraboloidal yield criterion is used to describe the yield in crystalline region, which is given by following Ref. [86]:

$$\varphi = \bar{\sigma}_B^2 - (\sigma_{yt} - \sigma_{yc}) I_1 - \sigma_{yt} \sigma_{yc}, \quad (15)$$

where $\bar{\sigma}_B$ is the equivalent von Mises stress $\bar{\sigma}_B = \sqrt{(3/2)\sigma'_B : \sigma'_B}$, σ'_B is the deviatoric part from the crystalline contribution, σ_{yc} and σ_{yt} are the corresponding yield stresses in compression and tension and $I_1 = \sigma_B : \mathbf{I} = -3p$ is the first invariant of the stress tensor. The yield stresses are extracted from the experimental hardening curve following the material identification procedure presented in Appendix A. Here, the mechanical response of crystalline region is assumed to be temperature-independent, thus according to the Clausius-Duhem entropy inequality for an isothermal process

$$\sigma_B : \dot{\mathbf{h}}_B - \dot{\psi}_B \geq 0 \quad (16)$$

where $\dot{\psi}_B$ is the time derivative of Helmholtz energy function in branch B. By considering the strain decomposition into elastic and plastic components, the above inequality can be rewritten as

$$\sigma_B : (\dot{\mathbf{h}}_B^e + \dot{\mathbf{h}}_B^p) - \left(\frac{\partial \psi_B^e}{\partial \mathbf{h}_B^e} : \dot{\mathbf{h}}_B^e + \frac{\partial \psi_B^p}{\partial a} \dot{a} \right) \geq 0 \quad (17)$$

where a is a strain-like parameter, whose increment Δa is related to equivalent plastic strain increment $\Delta \bar{\epsilon}^p = \sqrt{(2/3)\Delta \mathbf{h}_B^p : \Delta \mathbf{h}_B^p}$. The reduced internal dissipation can be written by defining the variable $\zeta = \partial \psi_B^p / \partial a$ as

$$\mathcal{D}_{int} := \sigma_B : \dot{\mathbf{h}}_B^p - \zeta \dot{a} \geq 0. \quad (18)$$

An optimisation problem is then formulated with this reduced internal dissipation inequality as

$$\mathcal{L}(\sigma_B, \zeta, \Delta \gamma) = -\mathcal{D}_{int} + \frac{\Delta \gamma}{\Delta t} \varphi, \quad (19)$$

where $\Delta \gamma$ is the Lagrange multiplier. The flow rule for the evolution of the plastic strain $\Delta \mathbf{h}_B^p$ and the internal strain-like variable a can be computed after solving

$$\frac{\partial \mathcal{L}}{\partial \sigma_B} = 0, \quad \frac{\partial \mathcal{L}}{\partial \zeta} = 0. \quad (20)$$

The plastic multiplier is the absolute solution of the quadratic equation which fulfils the Kuhn-Tucker's loading-unloading consistency conditions. The consistent elastoplastic tangent modulus is the tensorial differentiation of the updated stress from the radial return mapping derived with respect to associated and non-associated flow rules and follows

$$\mathbb{C}^{\text{ep}} = \frac{\partial \boldsymbol{\sigma}_{\text{B}}^{\text{tr}}}{\partial \mathbf{h}_{\text{B}}^{\text{tr,e}}} - \{\mathbb{C}^{\text{e}} : \mathbf{n}\} \otimes \frac{\partial \Delta \gamma}{\partial \mathbf{h}_{\text{B}}^{\text{tr,e}}} - \Delta \gamma \frac{\partial \{\mathbb{C}^{\text{e}} : \mathbf{n}\}}{\partial \mathbf{h}_{\text{B}}^{\text{tr,e}}}, \quad (21)$$

where 4th order tensors \mathbb{C}^{ep} and \mathbb{C}^{e} are the elastoplastic tangent modulus and elastic tangent modulus respectively. \mathbf{n} is the flow direction. The ":" operator stands for the double contraction mapping of a 2nd order tensor into 2nd order tensor and " \otimes " represents the dyadic product. The trial stress based on the prediction of total strain comprising elastic part is given by $\boldsymbol{\sigma}_{\text{B}}^{\text{tr}} = (\lambda_{\text{B}} \text{tr}[\mathbf{h}_{\text{B}}] \mathbf{I} + 2\mu_{\text{B}} \mathbf{h}_{\text{B}}) / \det[\mathbf{F}_{\text{B}}^{\text{e}}]$.

The inelastic deformation gradient $\mathbf{F}_{\text{B}}^{\text{p}}$ is updated as Eq. (6). The plastic deformation tensor $\mathbf{D}_{\text{B}}^{\text{p}}$ is given as follows

$$\mathbf{D}_{\text{B}}^{\text{p}} = \frac{\Delta \gamma}{\Delta t} \mathbf{n}, \quad \mathbf{n} = \frac{\partial \varphi}{\partial \boldsymbol{\sigma}_{\text{B}}}. \quad (22)$$

This framework is flexible to incorporate any specific crystal plasticity model. In case of rate-dependent behaviour of Resistance B, The micromechanical model considering crystallographic slip system [20] can be plugged in this framework to represent the fragmentation in crystalline phase.

5.3. Resistance C: network resistance

The rubbery effect was observed at different temperatures under large strain range in some TP (e.g., PMMA [66], PET [57], LDPE [22] and HDPE [35]) as well as in thermosets (e.g., Epoxy [74]). This effect, due to the reorientation of the molecular chains under large plastic deformation, was modelled considering a network resistance. A three-dimensional rubber elasticity spring system was developed to predict the evolution of anisotropy in an initially isotropic glassy amorphous polymers [87], then described by the non-Gaussian network theory combining the three- and eight-chain models [88]. To complete our proposed model (refer to Fig. 5), the mathematical formulation is briefly introduced below and its effect is studied in Appendix D. Due to the absence of the rubbery effect for the investigated nylon 101 and PA6, it is excluded for these two SCPs.

Recall that $\mathbf{F}_{\text{C}} = \mathbf{F}$, the internally stored backstress tensor \mathbf{B} that represents the network resistance is given by

$$\mathbf{B} = \sum_i B_i (\mathbf{e}_i \otimes \mathbf{e}_i), \quad (23)$$

where \mathbf{e}_i are the unit eigenvectors of the left Cauchy-Green stretch tensor $\mathbf{V}_{\text{C}} = \mathbf{F}_{\text{C}} \mathbf{F}_{\text{C}}^{\text{T}}$ and B_i are the principal back stress components. For the three-chains non-Gaussian network model, B_i has the following form

$$B_i^{\text{3-ch}} = \frac{1}{3} C^{\text{R}} \sqrt{N} \left[\lambda_i^{\text{p}} \mathcal{L}^{-1} \left(\frac{\lambda_i^{\text{p}}}{\sqrt{N}} \right) - \frac{1}{3} \sum_{j=1}^3 \lambda_j^{\text{p}} \mathcal{L}^{-1} \left(\frac{\lambda_j^{\text{p}}}{\sqrt{N}} \right) \right], \quad (24)$$

where λ_i^{p} is the plastic stretch on each chain in the network, \mathcal{L}^{-1} is the inverse Langevin function, and C^{R} and N are the rubbery modulus and the average number of links between entanglements, respectively.

An eight-chain model was also constructed with the corresponding principal components as

$$B_i^{\text{8-ch}} = \frac{1}{3} C^{\text{R}} \sqrt{N} \frac{\lambda_i^{\text{p}2} - \lambda^{\text{p}2}}{\lambda^{\text{p}}} \mathcal{L}^{-1} \left(\frac{\lambda^{\text{p}}}{\sqrt{N}} \right), \quad (25)$$

with

$$\lambda^p = \sqrt{\frac{1}{3} \sum_{j=1}^3 \lambda_j^{p2}}. \quad (26)$$

The full network model based on the orientation distribution of the individual chains provides the new principal stress components and it can be represented combining the aforementioned three-chains and eight-chains models as

$$\mathbf{B} = (1 - \kappa)\mathbf{B}^{3\text{-ch}} + \kappa\mathbf{B}^{8\text{-ch}}, \quad (27)$$

where κ is a weight factor defined as $\kappa = 0.85\lambda_{\max}^p / \sqrt{N}$ that depends on the maximal principal stretch $\lambda_{\max}^p = \max(\lambda_1^p, \lambda_2^p, \lambda_3^p)$ (see details in Ref. [88]).

6. Self-heating and dissipation

In this section, the deformation associated dissipation is considered as the heat source to derive the heat balance equation. The simplified model without viscoelastic response is used. The first thermodynamic principle for the local energy balance is stated as

$$\rho\dot{w} = \boldsymbol{\sigma} : \mathbf{D} - \nabla \cdot \mathbf{q} + \rho\phi, \quad (28)$$

where the scalars ρ , w and ϕ are the density, internal energy and external heat source, the vector \mathbf{q} represents the heat flux and $\boldsymbol{\sigma} : \mathbf{D}$ is the term of the rate of strain energy density. Noting that the Cauchy stress $\boldsymbol{\sigma}$ consists of three components (see Fig. 5), Eq. (28) is written as

$$\rho\dot{w} = \boldsymbol{\sigma}_A : \mathbf{L}_A^e + \boldsymbol{\sigma}_A : \mathbf{F}_A^e \mathbf{L}_A^p (\mathbf{F}_A^e)^{-1} + \boldsymbol{\sigma}_B : \mathbf{L}_B^e + \boldsymbol{\sigma}_B : \mathbf{F}_B^e \mathbf{L}_B^p (\mathbf{F}_B^e)^{-1} + \boldsymbol{\sigma}_C : \mathbf{L}_C - \nabla \cdot \mathbf{q} + \rho\phi. \quad (29)$$

The Clausius-Duhem inequality based on the second thermodynamic principle is given as

$$\rho\dot{s} + \nabla \cdot \frac{\mathbf{q}}{\theta} - \frac{\rho\dot{\phi}}{\theta} \geq 0, \quad (30)$$

where s is the specific entropy and θ is the material temperature. Considering the specific Helmholtz free energy $\psi = w - s\theta$, the Clausius-Duhem inequality can be rearranged as

$$-\rho\dot{\psi} - \rho\dot{s}\theta - \frac{\nabla \cdot \mathbf{q}}{\theta} + \boldsymbol{\sigma}_A : \mathbf{L}_A^e + \boldsymbol{\sigma}_A : \mathbf{F}_A^e \mathbf{L}_A^p (\mathbf{F}_A^e)^{-1} + \boldsymbol{\sigma}_B : \mathbf{L}_B^e + \boldsymbol{\sigma}_B : \mathbf{F}_B^e \mathbf{L}_B^p (\mathbf{F}_B^e)^{-1} + \boldsymbol{\sigma}_C : \mathbf{L}_C \geq 0. \quad (31)$$

Considering the Helmholtz free energy $\psi = \psi(\mathbf{C}_A^e, \mathbf{C}_B^e, \mathbf{C}_C, \theta)$ as a function of deformation and temperature of three branches in the rheological model. After several mathematical transformations, the derivative of ψ in terms of the Cauchy-Green tensor \mathbf{C}_π of different branches can be calculated as follows

$$\frac{\partial \psi}{\partial \mathbf{C}_\pi} : \dot{\mathbf{C}}_\pi = 2\mathbf{F}_\pi \frac{\partial \psi}{\partial \mathbf{C}_\pi} \mathbf{F}_\pi^T : \mathbf{D}_\pi. \quad (32)$$

The final form of the Clausius-Duhem inequality, therefore, can be written by substituting the above derivation in to Eq.(31) as

$$-\rho \left(j + \frac{\partial \psi}{\partial \theta} \right) \dot{\theta} + \left(\sigma_A - 2F_A^e \rho \frac{\partial \psi}{\partial C_A^e} F_A^{eT} \right) : D_A^e + \sigma_A : F_A^e L_A^p (F_A^e)^{-1} + \left(\sigma_B - 2F_B^e \rho \frac{\partial \psi}{\partial C_B^e} F_B^{eT} \right) : D_B^e + \sigma_B : F_B^e L_B^p (F_B^e)^{-1} + \left(\sigma_C - 2F_C \rho \frac{\partial \psi}{\partial C_C} F_C^T \right) : D_C - \frac{\nabla \theta}{\theta} \cdot \mathbf{q} \geq 0. \quad (33)$$

Following the constitutive equations fulfilled for any admissible deformation and temperature history, the Clausius-Duhem inequality in terms of the energy dissipation is obtained as

$$\sigma_A : F_A^e L_A^p (F_A^e)^{-1} + \sigma_B : F_B^e L_B^p (F_B^e)^{-1} - \frac{\nabla \theta}{\theta} \cdot \mathbf{q} \geq 0. \quad (34)$$

The relation represents the viscoplastic energy dissipation in branch A, the plastic energy dissipation in branch B and the thermal dissipation, respectively.

The heat equation can be derived from the first thermodynamic principle and the time derivative of the specific entropy j is given as

$$j = -\frac{\partial^2 \psi}{\partial \theta \partial C_A^e} : \dot{C}_A^e - \frac{\partial^2 \psi}{\partial \theta \partial C_B^e} : \dot{C}_B^e - \frac{\partial^2 \psi}{\partial \theta \partial C_C} : \dot{C}_C - \frac{\partial^2 \psi}{\partial \theta^2} \dot{\theta}. \quad (35)$$

Substituting j in the relation of $\dot{w} = \dot{\psi} + j\dot{\theta} + \dot{\theta}$ and using Eqs. (29) and (31), the heat equation can be obtained as

$$\rho c_p \dot{\theta} = \sigma_A : F_A^e L_A^p (F_A^e)^{-1} + \frac{1}{2} \frac{\partial \left((F_A^e)^{-1} \sigma_A (F_A^e)^{-T} \right)}{\partial \theta} : \dot{C}_A^e + \sigma_B : F_B^e L_B^p (F_B^e)^{-1} + \frac{1}{2} \frac{\partial \left((F_B^e)^{-1} \sigma_B (F_B^e)^{-T} \right)}{\partial \theta} : \dot{C}_B^e + \frac{1}{2} \frac{\partial (F_C^{-1} \sigma_C F_C^{-T})}{\partial \theta} : \dot{C}_C - \nabla \cdot \mathbf{q} + \rho \phi, \quad (36)$$

where the specific heat capacity $c_p = -\theta \partial^2 \psi / \partial \theta^2$ is used. The viscoplastic energy dissipation in amorphous phase and plastic energy dissipation in crystalline phase are represented by the two terms $\sigma_A : F_A^e L_A^p (F_A^e)^{-1}$ and $\sigma_B : F_B^e L_B^p (F_B^e)^{-1}$, respectively. The three terms representing the effect of thermo-mechanical coupling on the self-heating are ignored due to the small contribution compared to the (visco)plastic dissipation according to Ref. [73], leading to a reduced form by eliminating the external heat source term $\rho \phi$. The above equation yields

$$\rho c_p \frac{\partial \theta}{\partial t} = \underbrace{\sigma_A : F_A^e L_A^p (F_A^e)^{-1} + \sigma_B : F_B^e L_B^p (F_B^e)^{-1}}_{\text{heat source associated with deformation}} - \nabla \cdot \left(-k \frac{\partial \theta}{\partial x} \mathbf{x} \right), \quad (37)$$

where k is the thermal conductivity. The temperature increase is attributed to the plastic dissipation. At every call of the mechanical model, the rate of plastic dissipation is calculated and fed back to the heat equation, making it possible to capture the self-heating effects.

7. Numerical implementation

In this section, the proposed model is integrated as user-defined material model for the finite element method (FEM) considering fully TMC analysis. The activation and disclosure of the crystalline contribution (resistance B) is also addressed.

7.1. Thermomechanical coupling

Fully TMC analyses were conducted using a single element test, cylinder compression and dog-bone tension models. The description of these models are presented in Section 8, accompanied with the corresponding results.

Fig. 6 shows the TMC framework and the activation of the crystalline contribution in the proposed model. Self-heating and heat transfer are considered in the simulations, where the temperature and the stress fields are determined simultaneously during every time increment. A user-defined thermal model was implemented along with the user-defined mechanical model to update the temperature field by solving the energy balance equation in every increment. The influence of temperature can affect the mechanical response in two ways: (1) temperature-dependent elastic modulus, which is calibrated with respect to the one at reference temperature and (2) temperature-dependent viscoplastic constitutive model.

439
440
441
442
443
444
445

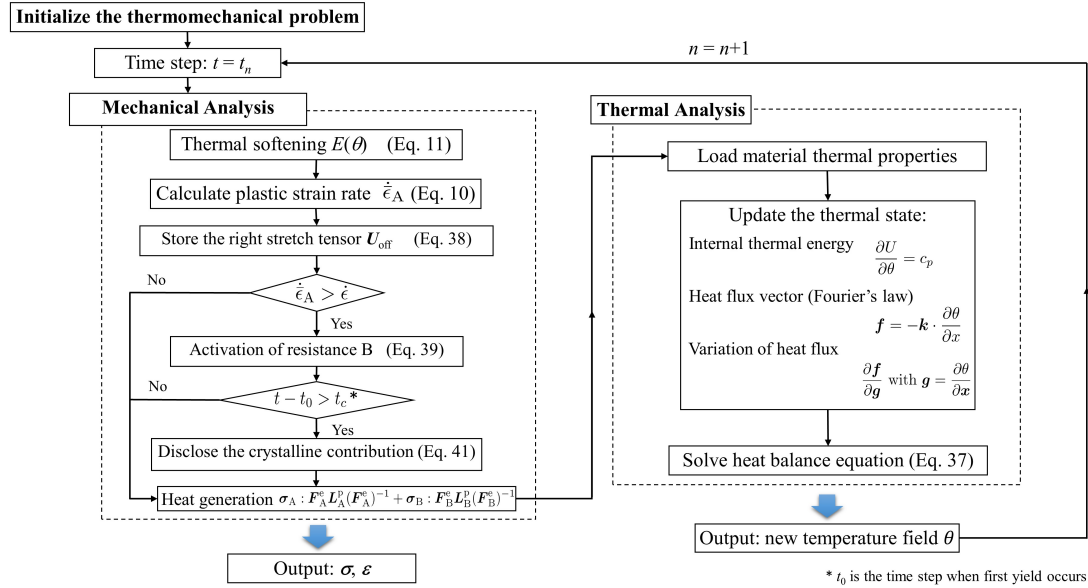


Figure 6: Flowchart of double yield model in a fully coupled thermomechanical analysis.

Three regimes, namely isothermal, $\dot{\epsilon}$, coupled and nearly adiabatic, can be identified depending on the ratio between the approximated thermal diffusion time and the test time at different strain rates [66]. A full analysis covering these three regimes is essential for SCPs because of the strong temperature dependence of the mechanical response [2]. Chen *et al.* [72] investigated the temperature evolution for PA6 under uniaxial loading. Under monotonic tensile tests, the temperature initially experiences a slight drop due to the thermoelastic effect and then follows an increase attributed to self-heating. At high strain rate of 1 s^{-1} , for instance, the tests generally can be conducted within a short period and this is insufficient to diffuse the accumulated temperature. Consequently, thermal softening occurs due to temperature sensitivity.

446
447
448
449
450
451
452
453

7.2. Activation of crystalline contribution

In order to quantitatively characterize the first yield and disclose the crystalline contribution, the exact moment to activate the crystalline phase has to be decided based on a physically-based argument. To control the activation of the crystalline contribution, the right stretch tensor \mathbf{U} is continuously stored (see Fig. 6). Once the condition of first yield in amorphous phase is fulfilled (at the time $t = t_0$), an internal variable \mathbf{U}_{off} is assigned as follows

454
455
456
457
458

$$\mathbf{U}_{\text{off}} = \mathbf{U}_{t=t_0} = \mathbf{R}^{-1} \mathbf{F}. \quad (38)$$

This internal variable \mathbf{U}_{off} is adopted to offset the deformation gradient and the new deformation gradient \mathbf{F}_B imposed on crystalline phase is updated by

459
460

$$\mathbf{F}_B = \mathbf{R}(\mathbf{R}^{-1} \mathbf{F} - \mathbf{U}_{\text{off}}) + \mathbf{I}. \quad (39)$$

Table 1

Thermal properties of nylon 101, LDPE, polyamide 6, circular compression discs and grips, obtained from the online material database www.goodfellow.com and www.ensingerplastics.com

	ρ (kg/m ³)	c_p (J/kg K)	k (J/s m K)
Nylon 101	1150	1500	0.36
LDPE	919	2600	0.32
Polyamide 6	1200	1700	0.25
Steel	7800	420	52

It is believed that there exists an internal drag stress or friction stress considering plastic flow as rate-dependent [89]. In SCPs, these stresses can be attributed to the interaction between the amorphous polymer chains and the crystalline lamellar blocks. According to the stage III in Fig. 4, the flow stress of the amorphous phase experiences the strain softening once the first yield is reached, what it adds a delay before revealing the crystalline contribution. A characteristic time t_c is introduced to quantitatively regulate the adjustment between these two phases during this period. The determination of t_c is illustrated and validated in Appendix B. The strain ϵ_c required to observe the apparent linear elastic segment of crystalline phase depends on t_c and the relation $\epsilon_c = t_c \dot{\epsilon}$ holds. At a high strain rate, the test time is short and even a small characteristic time t_c results in a certain amount of strain to establish the equilibrium of two phases, where a "small hump" is observed in stress-strain curve. However, at a low strain rate, a large characteristic time t_c may lead to a negligible strain ϵ_c between the first yield and the initiation of the crystalline contribution. Once the internal equilibrium is achieved when the time interval equals t_c , the stress contribution of the crystalline phase is rescaled by a factor α . This factor is updated by

$$\alpha = \frac{\sigma_{B,eq} - \sigma_{off}}{\sigma_{B,eq}}, \quad (40)$$

where σ_{off} is the equivalent stress at the disclosure point ($t = t_0 + t_c$) and $\sigma_{B,eq}$ the current equivalent stress. The investigation of the amorphous phase and the activation of the crystalline phase in nylon 101 are documented in Appendix B. The updated stress $\sigma_{B,cor}$ from crystalline phase is calculated as follows

$$\sigma_{B,cor} = \alpha \sigma_B. \quad (41)$$

8. Results and discussion

Three SCPs showing the DY phenomenon, nylon 101 and LDPE in compression [12, 22] and PA6 in tension [29], were chosen to validate the proposed model. Tests were conducted under different strain rates, which are suitable to validate the reliability of the model, as well as the self-heating and thermal softening effects. The parameter identification (PI) procedure can be found in Appendix A. The TMC analyses were carried out using a realistic cylinder compression test and dog-bone tension test to validate the response of nylon 101, LDPE and PA6, respectively.

8.1. Response under compression

A 3D finite element model of a cylinder uniaxial compression test at room temperature was developed. An implicit solver was used to study the full range of the thermomechanical response. A combination of a user-defined mechanical and thermal material is employed. The thermal properties are listed in Table 1. Fig. 7 shows the setup and the one-eighth FEM model with the simplifications according to the symmetry. The model was meshed using 8-node thermally coupled elements. Mesh sensitivity was conducted to check mesh convergence, where an element length of 0.5 mm and 0.2 mm proved to provide convergent results for nylon 101 and LDPE, respectively.

Frictionless contact and same thermal conductivity were applied between the cylinder specimen and the compression discs. Two steps were introduced to preheat the model to 22°C prior to applying the compressive load. The displacement control loading along y-axis was applied to the reference point (RP), which was connected to the upper disc by a rigid constraint. Once the second loading step began, the preheat temperature boundary condition (BC) was deactivated and a convection film coefficient $h = 10 \text{ W}/(\text{m}^2 \text{ C})$ was imposed on the outer surface in contact

with the surrounding medium. The true stress-strain curve was obtained from the model using the volume-averaged homogenized values as follows

$$\sigma_{\text{homg.}} = \frac{1}{V} \int \sigma dV \approx \frac{\sum_{i=1}^{n_{\text{elem}}} \sigma_i V_i}{V}$$

$$\epsilon_{\text{homg.}} = \frac{1}{V} \int \epsilon dV \approx \frac{\sum_{i=1}^{n_{\text{elem}}} \epsilon_i V_i}{V}$$
(42)

where σ_i , ϵ_i , and V_i are the stress, strain and volume of the i -th element and V is the volume of the one-eighth specimen.

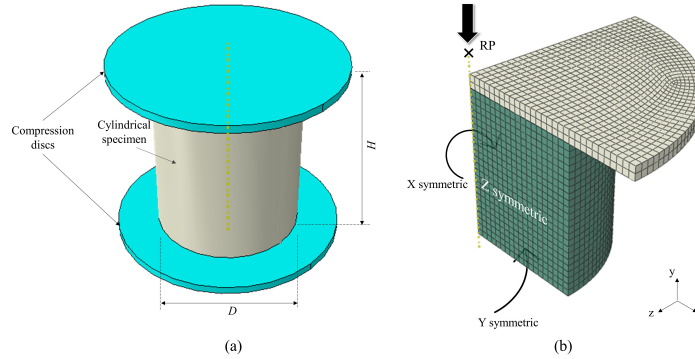


Figure 7: FEM of the cylinder compression test setup: (a) geometry, and (b) one-eighth model, mesh and BC.

8.1.1. Case of nylon 101

The cylinder has a diameter of 19.1 mm and height of 22.9 mm. The model mesh contains 9,637 linear hexahedral elements. Rubber effect represented by the network resistant C is neglected according to the experimental stress-strain curves.

Stress-strain curves

Fig. 8 shows the homogenized stress-strain curves of three datasets: (i) symbols, experimental data from [12], (ii) grey lines, single element (SE) test, used to develop and debug the present model and (iii) black lines, the simulation results of the cylinder model.

The DY phenomenon is captured by the proposed model with the first yield at a strain around 6% and the second yield at 16.5%. The rate-dependent $\sigma_{y,I}$ is generated from amorphous intermolecular resistance A. At this stage the difference between SE and cylinder results is negligible. The predicted first yield stresses are 79.5 MPa, 99.0 MPa and 115.6 MPa at the temperature of 22°C when the strain rate increases from $1 \times 10^{-5} \text{ s}^{-1}$ to $1 \times 10^{-2} \text{ s}^{-1}$ to 1 s^{-1} (see Fig. 8(a)). Compared to the experimental results, the errors are 2.71%, 1.59% and 1.50%, respectively. The "small humps" are disclosed except for the quasi-static case ($\dot{\epsilon} = 1 \times 10^{-5} \text{ s}^{-1}$), thanks to the introduced characteristic time t_c . The corresponding predicted strains ϵ_c between the first yield and the local lowest stress level are 3.07% and 4.35% at the strain rate of $1 \times 10^{-2} \text{ s}^{-1}$ and 1 s^{-1} , whereas the experimental values are 1.5% and 3.0%. The faster the test, the larger ϵ_c . The predictions from the SE and the cylinder tests begin to deviate as the plastic strain increases, and the discrepancy appears after the $\sigma_{y,II}$. The self-heating and thermal softening effects are taken into account so that the $\sigma_{y,II}$ can be predictable under different thermomechanical conditions.

Fig. 8(b) shows the comparison at the temperatures of 22°C and 66°C. The stress-strain curves at a moderate strain rate of $1 \times 10^{-2} \text{ s}^{-1}$ are chosen to present the temperature-dependence. Because the equilibrium between amorphous and crystalline phases can be easily established at a higher temperature, the t_c equals to zero regardless of the applied strain rate at 66°C. The proposed model captures well the stress-strain curve with the self-heating and thermal softening effects. The difference between experimental and simulated ones above the strain 50% may due to the simplified logarithmic relation between the elastic modulus and the temperature via a constant β (see Eq. (11)), which is unable to represent the realistic one. Instead, a DMA-based temperature sweep test is highly recommended to obtain a realistic

Table 2

Three thermomechanical regimes in the cylinder specimen at different strain rates.

$\dot{\epsilon}$ (s^{-1})	$t_{\text{test}}/t_{\text{diff}}$	thermomechanical regime
10^{-5}	202	nearly isothermal
10^{-4}	20.2	coupled
10^{-3}	2.02	coupled
10^{-2}	0.202	coupled, approaching adiabatic
1	0.00202	adiabatic

$E_A(\theta)$. The augmentation of the temperature and the softening of material are controlled by the parameters h and β . A parametric study along with their underlying physical interpretation is presented in Appendix E.

In addition, the internal temperature field is impossible to be measured experimentally during the test, and it is highly related to the material state due to the thermal softening. In that sense, the simulation results can provide valuable insights within the sample.

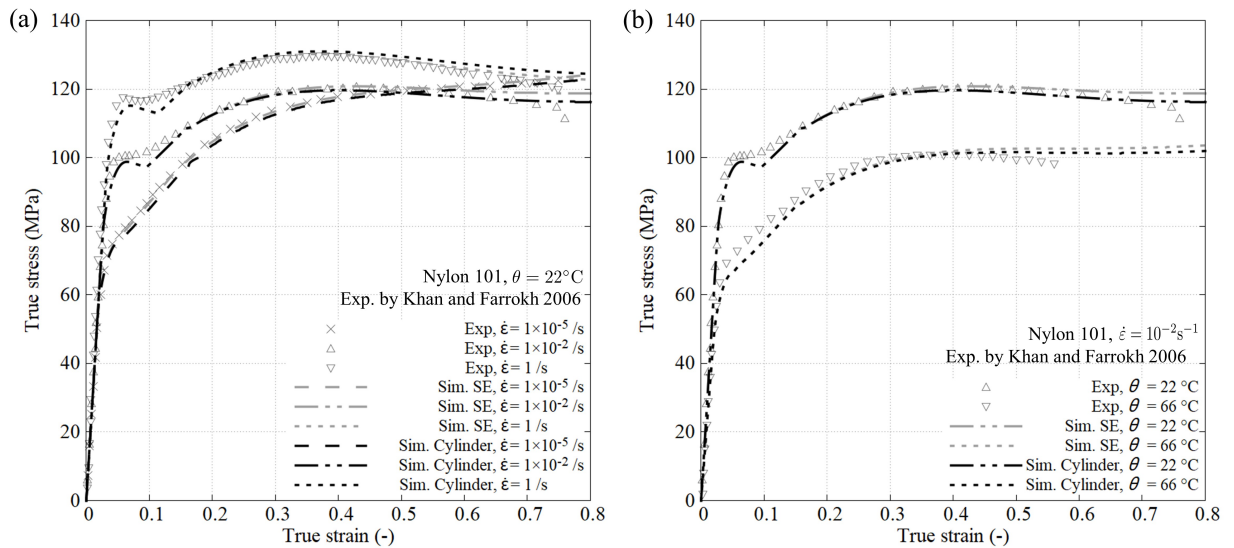


Figure 8: Comparison between experimental results of nylon 101 [12] and the prediction of the proposed thermomechanical model using a realistic cylinder compression specimen and single element model.

Investigation of self-heating

Fig. 9-11 shows the true stress-strain curves along with the evolution of the temperature. The internal temperature field is shown on the right by mirroring the one-eighth model. Three strains were selected to investigate the temperature field: at the first yield, the second yield and a true strain of 75%. The self-heating and thermal softening is examined numerically in three representative regimes: isothermal, coupled and nearly adiabatic. The three regimes corresponds to the ratio of the test period ($t_{\text{test}} = \epsilon/\dot{\epsilon}$) and the thermal diffusion time t_{diff} . (see Table 2). This diffusion time can be estimated using the thermal diffusivity and the characteristic length of the specimen calculated from the centre of the deforming region to the nearest heat sink [66].

Fig. 9 shows that the average surface temperature remains despite of the wide strain range. The test period under an isothermal condition with strain rate $\dot{\epsilon} = 1 \times 10^{-5} s^{-1}$ lasted around 21 hours. This long period allows heat diffusion that leads to increase the temperature from 22°C to 23.2°C . However, under a coupled condition ($\dot{\epsilon} = 1 \times 10^{-2} s^{-1}$), the average surface temperature can reach 49.8°C at 75% of strain. Additionally, the compression discs experience a visible rise of temperature, as Fig. 10 shows. Under a nearly adiabatic condition ($\dot{\epsilon} = 1 s^{-1}$), the loading time reduces to 0.75 s, which is insufficient to decrease the temperature rise caused by the self-heating from the specimen. The heat cannot even be sufficiently conducted to the compression discs as Fig. 11 shows.

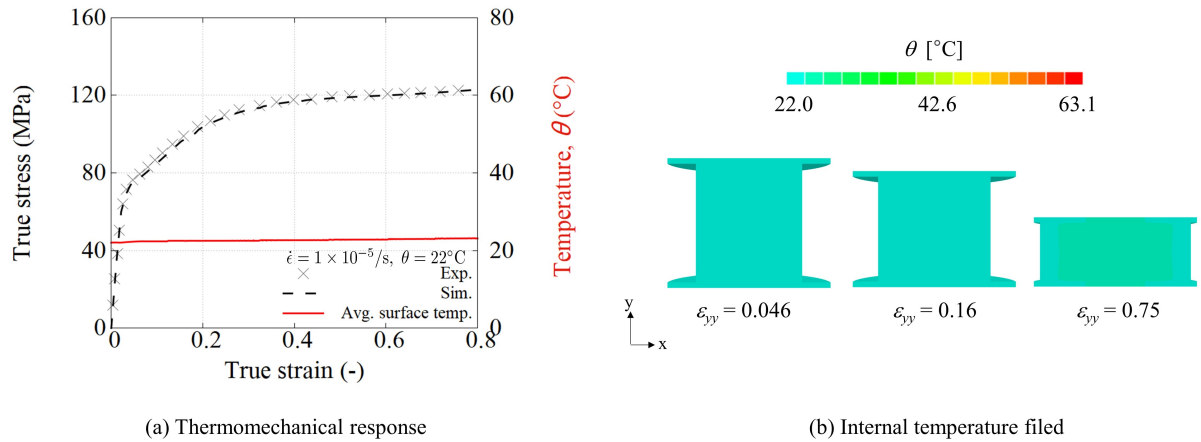


Figure 9: (Color online) Thermomechanical response of nylon 101 and temperature evolution at strain rate of $1 \times 10^{-5} \text{ s}^{-1}$: (a) average temperature on the outer curved surface and (b) internal temperature field in the midplane of the sample.

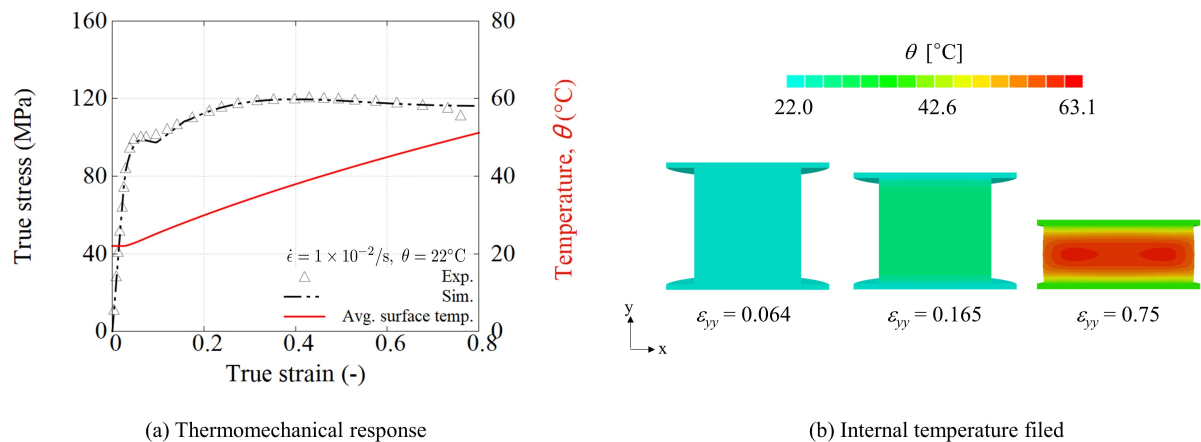


Figure 10: (Color online) Thermomechanical response of nylon 101 and temperature evolution at strain rate of $1 \times 10^{-2} \text{ s}^{-1}$: (a) average temperature on the outer curved surface and (b) internal temperature field in the midplane of the sample.

In general, higher temperature is found in the core region compared to the one from specimen surfaces (63.1°C compared to 60.2°C at 75% under $\dot{\epsilon} = 1 \text{ s}^{-1}$, Fig. 11). Also, Fig. 10 and 11 show that temperature field within the cylinder specimen is not homogeneous. As the amorphous intermolecular resistance A is highly temperature-dependent, the occurrence of thermal softening results to a different thermomechanical response on each material point due to the inhomogeneous plastic deformation field.

8.1.2. Case of LDPE

Same experimental setup of cylinder compression specimen was adopted to characterize the rate-dependent mechanical response of LDPE under large deformation [22]. The cylindrical specimen is 5 mm in diameter and length. Rubber effect can be observed from the macroscopic stress-strain curves. The complete model with three components is used for the validation. The identified parameters are listed in Table A.1 and A.2. The thermal properties adopted is provided in Table 1. The eight-chain network model ($\kappa = 1$) is considered in this Section.

Fig. 12 shows the comparison between the experimental and simulated results at 22°C . Both the rubber effect and DY phenomenon are well captured for two different strain rates: 0.01 s^{-1} and 0.2 s^{-1} . The first yield occurs around a strain level of 10% , while the second yield 40% . The rubber effect results in a nonlinear stress increase, which is also predicted around a strain of 80% . Furthermore, the self-heating and thermal softening effects lead to the drop trend in

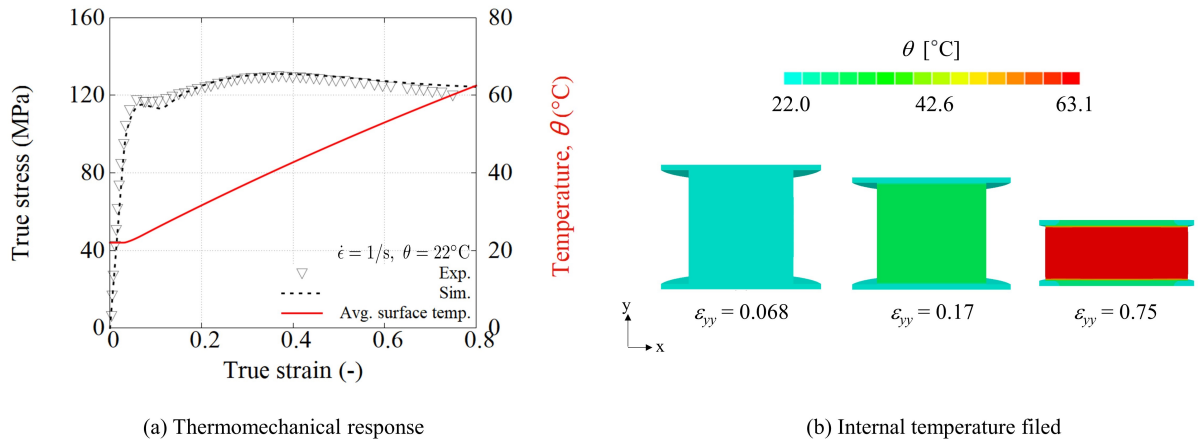


Figure 11: (Color online) Thermomechanical response of nylon 101 and temperature evolution at strain rate of 1 s^{-1} : (a) average temperature on the outer curved surface and (b) internal temperature field in the midplane of the sample.

stress-strain curve at the strain rate of 0.2 s^{-1} . However, a difference can also be found in cylinder and SE tests. The average temperature in cylinder specimen is relative lower than in SE model due to the metallic discs attached to the specimen. The temperature decreases as the heat is efficiently conducted. The inhomogeneous temperature field in the cylinder specimen alters the mechanical response due to less thermal softening effect. Therefore, higher stress level is seen in the cylinder test. A parametric study of rubber effect combining DY phenomenon at different strain rates can be found in Appendix D.

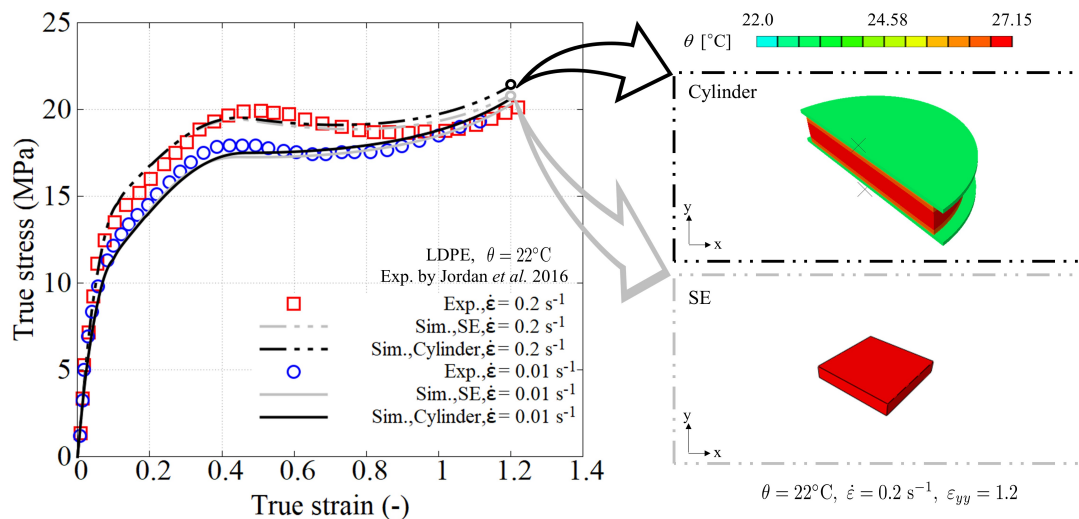


Figure 12: Comparison between experimental results of LDPE [22] and the prediction of the proposed thermomechanical model using a realistic cylinder compression specimen and single element model.

8.2. Response under tension

The experimental results for PA6 extracted from Ref. [29] was used to validate the proposed model under tension. The adopted polymer is mainly composed by α -I phase, from which a dog-bone specimen was proposed and dry-conditioned. Due to possible necking, the geometrical nonlinearity along with the plastic deformation can magnify the yield drop [74]. The experimental data is available in the form of engineering stress-strain, however, the PI process

requires true stress-strain. Therefore, logarithmic strain is adopted assuming constant volume and constant Poisson's ratio, the true stress is given by $\sigma_{\text{true}} = F/A_0 \cdot e^{\epsilon_x}$.

8.2.1. Case of Polyamide 6 (PA6)

In order to compare to the experimental results, a FEM model to simulate the ISO527 standard using a 1BA type dog-bone specimen was developed. The dimensions of the 1BA dog-bone are presented in Fig. 13(a). This specimen has a gauge zone of 22 mm \times 5 mm and 5 mm thickness. Four rectangular tabs are connected to the specimen using tie constraints to mimic the attached grips. Contact conduction for the TMC analysis was modelled. Following the standard ISO527-2, the initial distance between grips was chosen larger than the distance between broad parallel-sided portions with a difference of 2 mm. To reduce the calculation cost, symmetry along y-axis was applied. Fig. 13(b) shows the thermomechanical BCs on a meshed geometry with a global element length of 0.25 mm (mesh convergence was checked). The natural convection coefficient $h = 20 \text{ W}/(\text{m}^2 \text{ C})$ was imposed on the surface between the grips except for the symmetrical internal surface. A contact conductance of $52 \text{ J}/\text{s m K}$ was assigned to the contact surfaces. Two tabs on the left were fixed, whereas tabs on the right were connected to a RP. Equation type constraints were used to couple their DOF and synchronize the movement. The displacement along x-axis was imposed to the RP. To ensure that the applied strain rate is consistent with experimental one, the input strain rate is calculated according to the gauge length. Coupled temperature-displacement element is used with reduced integration and enhanced hourglass control. The half model is composed of 4,120 linear hexahedral elements and 7,513 nodes.

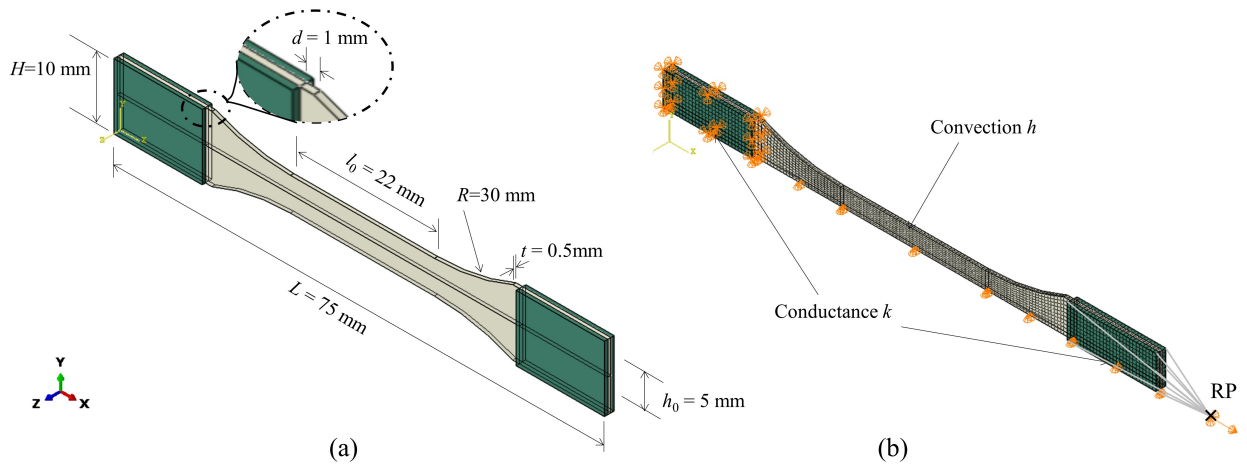


Figure 13: FEM of the dog-bone tension test setup: (a) geometry, and (b) symmetrical model, mesh and BC.

Stress-strain curves

Unlike Section 8.1, the dog-bone results are based on the engineering values of the stress and strain. The engineering stress is calculated by the reaction force F_{RP} from RP divided by the initial cross-section area of the gauge zone ($A_0 = 0.5 \text{ mm} \times 5 \text{ mm}$). The engineering strain is obtained using the gauge length $l_0 = 22 \text{ mm}$ as reference. The distance between two nodes are tracked and divided by l_0 .

Fig. 14 presents the model results under isothermal and fully TMC regimes at different strain rates. It can be noticed that the stress-strain hump is also clearly captured in this test configuration. The model predicts the $\sigma_{y,I}$ at strain around 4% and leading to an increase of peak stress from 74 MPa up to 84 MPa as the strain rate increases from 10^{-4} s^{-1} to $3 \times 10^{-3} \text{ s}^{-1}$. Under isothermal condition, the stress-strain curves obtained from the model (Fig. 14(a), lines) follow the same trend at different strain rates, leading to a group of parallel curves. This is due to two reasons: (1) the rate dependency is carried out only by the amorphous phase, which reaches a clear stable saturated state of plastic flow [74], and (2) the contribution of the rate- and temperature-independent crystalline phase remains unaltered and only adds up the plastic hardening.

Fig. 14(b) shows the model results considering full thermomechanical coupling. In this case, it can be seen that the curves at the highest $\dot{\epsilon}$ dropped due to a clear thermal softening occurred in the amorphous phase. This result indicates that the self-heating process cannot be ignored as it leads to an excellent agreement with the experimental

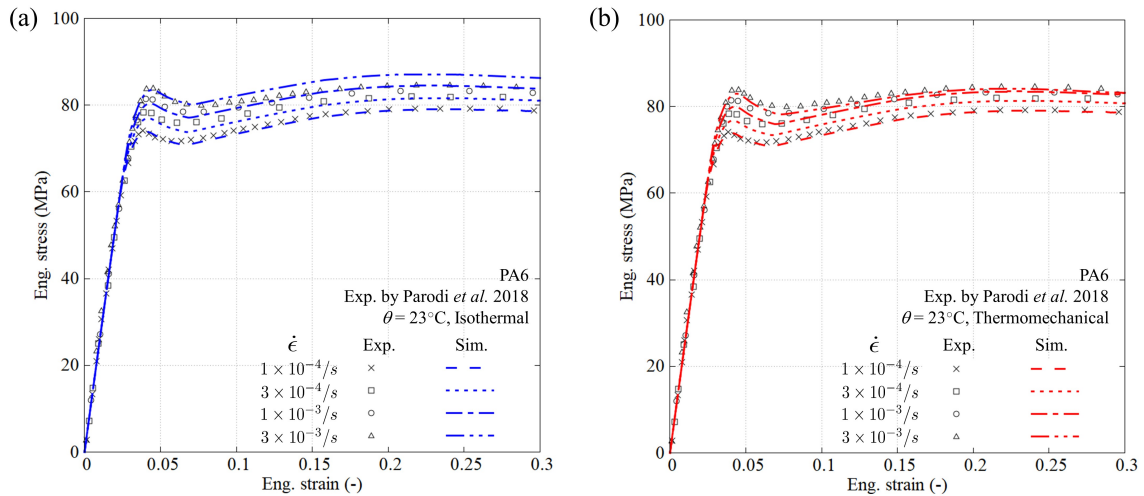


Figure 14: Comparison between experimental results of PA6 and the prediction with realistic dog-bone tension specimen: (a) isothermal analysis and (b) fully coupled thermomechanical analysis.

observations. On top of that, it is worth mentioning that the effect of temperature on the elastic modulus shall also be properly measured. The crystallization temperature θ_c for PA6 is around 170°C and the accumulated temperature via self-heating during the test cannot reach the crystallization temperature θ_c . Therefore, the effect of thermal softening on the crystalline phase is not considered. This fact can facilitate the PI process using an identical crystalline contribution at any strain rates and temperatures below θ_c .

Investigation of necking and self-heating

Fig. 15 shows the comparison of isothermal and TMC cases in terms of effective plastic strain and temperature fields. Necking process is also illustrated where the thermal softening plays an important role. In the present model, four strains were chosen: 4.4% corresponding to the $\sigma_{y,I}$, 22% to the $\sigma_{y,II}$, 36% and 45% (a larger strain to demonstrate the necking under a well-developed self-heating). Nitta and Kuriyagawa [30] observed for metallocene-catalyzed HDPE that necking is usually initiated between both yield points and got stabilized at the second yield where the fragmentation of crystalline lamellar clusters occurs. A locally closed-packed layer structure was formed and an inhomogeneous plastic strain field was observed in the transition zone between the narrow parallel- and curved-sided portions.

At 4.4%, the amorphous region starts to yield. The temperature field in the gauge zone increased slightly and the maximum effective plastic strain in thermal coupled analysis is higher. At 22%, the neck is stabilized at the second yield, showing a more homogeneous effective plastic strain field. At 36%, the temperature continues to increase but with a relative slow speed due to the preferred thermal parameters (h and β). The maximum effective plastic strain in the thermal coupled analysis is 0.36, which is quite large compared to the one in isothermal condition (0.30). Besides, its corresponding contour affected by the temperature field can be clearly seen with more concentrated region within the gauge zone. At 45%. An obvious macroscopic neck can be observed in the coupled case with a maximum effective plastic strain of 0.54 (0.39 in the isothermal analysis). The temperature increased more than 4°C , being sufficient to speed up the necking.

Kweon and Benzerga [90] investigated the mesh size effect on shear band taking place in a dogbone experiencing necking under isothermal condition. The viscoplastic glassy amorphous polymer model with a parameter set ($s_2/s_1 = 0.61$ and $s_1/s_0 = 1$ for a sharp yield point) was used to increase the propensity to shear banding. However, with the identified parameter set for the PA6, no sharp transition was found around $\sigma_{y,I}$. Therefore, shear band is not obvious in the present model (see Fig. 15). Although the strain softening is mainly characterized by the constitutive model within the strain range from 4% to 7%, the neck initiation and evolution also affect the predicted nominal stress-strain curves. In addition, a temperature increase due to self-heating accelerates the necking process affecting even more the mechanical properties.

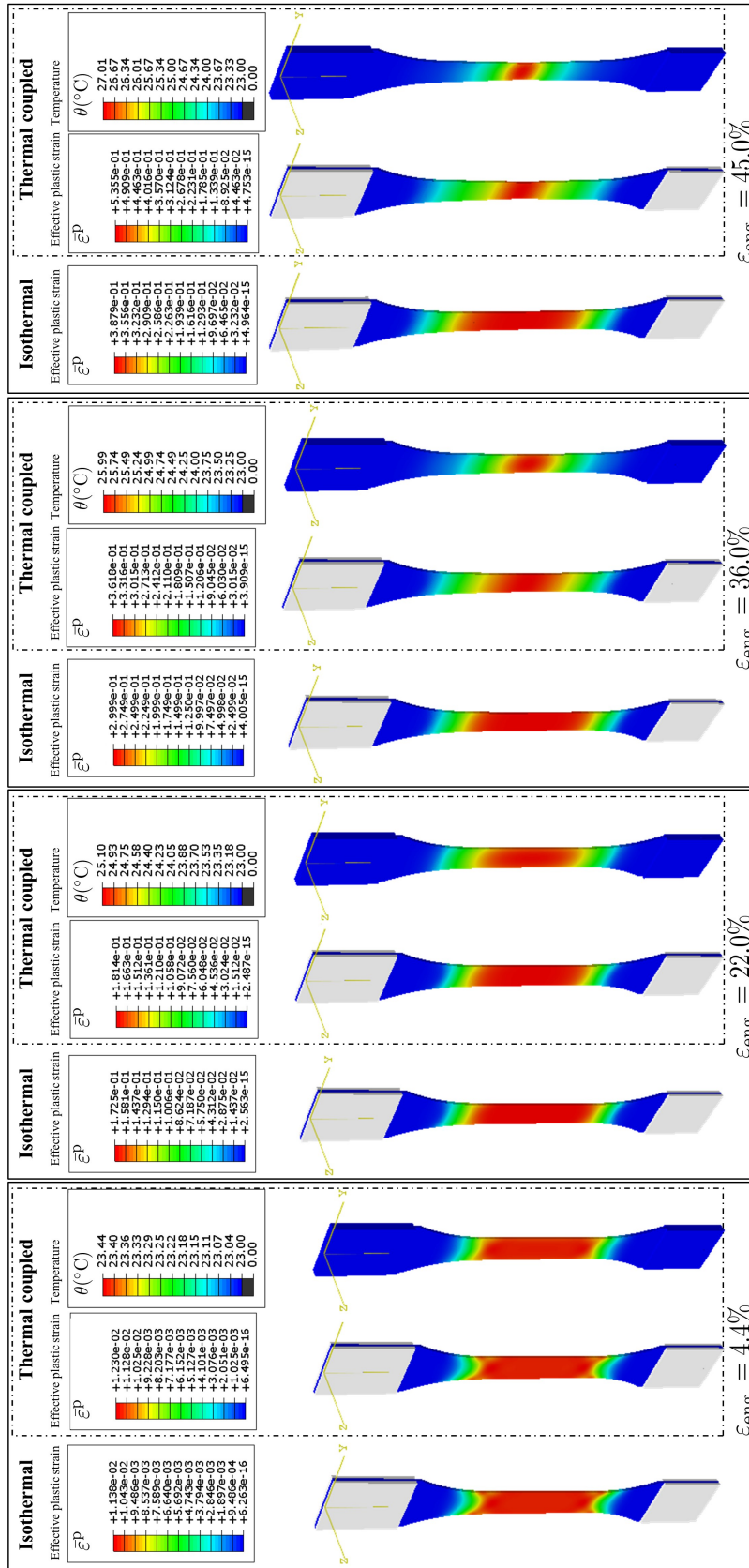


Figure 15: (Color online) Necking process in the dog-bone tension specimen in terms of effective plastic strain and temperature fields between isothermal analysis and fully TMC analysis.

9. Conclusion

The proposed viscoelastic-viscoplastic-hyperelastic model based on three types of resistances is capable to accurately capture the DY phenomenon and the strain-rate-triggering self-heating. A good agreement has been found between the experimental and simulation results in a wide strain range. The contribution of this work includes:

- A straightforward and robust PI procedure. The same minimum set of experiments is required as the modified BPA model and only one hardening curve for the crystalline contribution needs to be extracted. The PI process is used to capture the response of the thermoplastic nylon 101, LDPE and PA6 at different strain rates with high fidelity.
- The yield kinetics of SCP was reviewed and the morphological changes of the blended crystalline and amorphous phases were lumped and interpreted with a switch. A characteristic time t_c was introduced to control the activation and to disclose the crystalline contribution, leading to the formation of "small humps" similarly observed in the tests.
- The cylinder compression test was simulated for nylon 101 and LDPE under a full TMC regime, where rubber effect was activated for LDPE. Both SE and cylinder tests generate satisfactory results. The self-heating and thermal softening triggered by the strain rate were accurately captured. Additionally, the influence of the thermal parameters, namely the inelastic heat fraction η , temperature-dependent β and convection coefficient h , on the mechanical behaviour were discussed using a SE analysis. The stress-strain curves move downwards when increasing η and β , or decreasing h . Further experimental study is required to determine a correct combination of these parameters by cross checking the surface temperature field.
- A dog-bone tension model was used for PA6 validation to study the initiation and evolution of necking. Results show that the self-heating and thermal softening effects accelerate the necking process. The temperature fields were investigated in a full TMC regime, leading to clear inhomogeneous deformation patterns.
- The flexibility of this modular constitutive model was studied that offers the possibility of incorporating the viscoelastic response. The parametric study shows that the simulated stress-strain curves can be either used for thermoplastics or thermosets. The advantages of the proposed model lead to less effort in material characterization that allows for decoupling the viscoelastic response from the other features, whose parameters can be identified independently. On top of that, more complex loading types are required for the model validation, for instance, considering the unloading curve of SCPs with obvious nonlinearities and hysteresis loops.

CRedit authorship contribution statement

P. Hao: Conceptualization, Methodology, Software, Investigation, Validation, Writing - original draft, Writing - review & editing, Visualization. **V. Laheri:** Software, Validation, Writing - review & editing. **Z. Dai:** Software, Validation, Writing - review & editing. **F. A. Gilabert:** Conceptualization, Methodology, Software, Supervision, Funding acquisition, Writing - review & editing.

Acknowledgements

The work leading to this abstract has been funded by the ICON project "ProPeL" (HBC.2019.0094), which fits in the MacroModelMat (M3) research program, coordinated by Siemens (Siemens Digital Industries Software, Belgium), and funded by SIM (Strategic Initiative Materials in Flanders) and VLAIO (Flemish government agency Flanders Innovation & Entrepreneurship). Financial support from "Bijzonder Onderzoeksfonds" (BOF.STG.2018.0030.01) by Ghent University is also gratefully acknowledged. The authors extend their sincerest gratitude towards the reviewers' insightful comments, suggestions and recommendations that were highly influential in improving the quality of this paper.

Appendices

670

A. Mechanical model parameters

671

This Appendix summaries the parameter identification stages for the proposed double yield model using the thermoplastic nylon 101 as example. To characterize the intrinsic response, true stress-strain curves should be used. For a non-isothermal case with various strain rates, the amorphous contribution follows the exhaustive calibration steps provided in Ref. [74]. This procedure leads to a unique parameter set accounting for various strain rates and temperatures, which is briefly illustrated as follows:

672

673

674

675

676

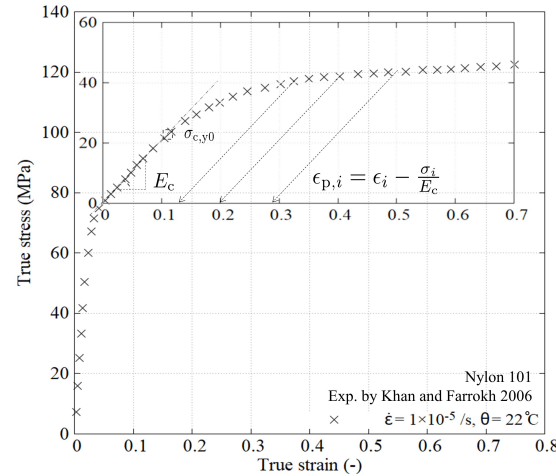


Figure A.1: Experimental stress-strain curve at low strain rate $1 \times 10^{-5} \text{ s}^{-1}$ and its decomposition into amorphous and crystalline contribution.

1. **Baseline curve:** The stress-strain curve at the lowest available strain rate ($\dot{\epsilon} = 1 \times 10^{-5} \text{ s}^{-1}$) was chosen as the baseline. Under quasi-static loading condition, the thermal effect is negligible, therefore the isothermal mechanical response can be obtained. 677
2. **Decomposition:** The stress-strain curve can be decomposed into amorphous and crystalline contributions (see Fig. A.1). A sub-window with an offset origin is imposed where the transition from the nonlinearity to a linear elastic response (apparent crystalline initiation) is found. 678
3. **Amorphous contribution:** Using the modified BPA model perform the calibration with a set of stress-strain curves before reaching the apparent linear region. Readers are referred to follow the same procedure as in [74]. In the case of nylon 101, the curve shape was determined according to the one at the strain rate of $\dot{\epsilon} = 1 \times 10^{-5} \text{ s}^{-1}$, where the parameters $E_{a,\text{ref}}, \theta_{\text{ref}}, \nu_a, s_0, s_1, s_2, h_1, h_2, \bar{\epsilon}_p, f, m, \bar{\epsilon}_0$ and A were identified with the minimum required tests (see Table A.1). The temperature-dependent modulus was determined with a logarithmic law via $\log(E_{\text{ref}}/E(\theta)) = \beta(\theta - \theta_{\text{ref}})$. 679
4. **Crystalline contribution:** Perform the calibration using one single stress-strain curve in the sub-window. An elastoplastic response was assumed for the investigated nylon 101. The apparent elastic modulus E_c and initial yield stress $\sigma_{c,y0}$ can be obtained using a linear relation. The hardening data was generated by imposing $\epsilon_{p,i} = \epsilon_i - \sigma/E_c$ in the plastic region (listed in Table A.2). 680
5. **Activation of the crystalline phase:** Once the $\sigma_{y,1}$ in amorphous domain is achieved, the crystalline contribution must be activated. A rate-dependent characteristic time t_c is introduced to disclose the apparent contribution, resulting in a curve with a "small hump" at high strain rate (see Appendix B). 681
6. **Thermomechanical coupling:** Constant thermal properties of the SCP and compression discs (tension grips) were assumed (Table 1). The self-heating and thermal softening effects on stress-strain curves were determined via the parameters h and β (refer to Appendix E for the parametric study). The convection parameter h was approximated at any moderate strain rate under thermal coupled condition. 682

683

684

685

686

687

688

689

690

691

692

693

694

695

696

697

698

699

Table A.1

Set of mechanical parameters of the double yield model for the amorphous and crystalline components.

Material parameter	Unit	Description	Nylon 101	PA6	LDPE	Eqn.
Amorphous						
$E_{a,ref}$	GPa	Modulus at θ_{ref}	3.01	2.62	225	(11)
θ_{ref}	K	Reference temperature	295	296	295	(11)
β	1/K	Temperature dependence	0.0022	0.0036	0.0234	(11)
ν_a	-	Poisson's ratio	0.39	0.39	0.42	(11)
s_0	MPa	Initial equivalent strength	120	184	28	(11)
s_1	MPa	Athermal peak strength	140	196	34	(12)
s_2	MPa	Saturation strength	138	193	34	(12)
h_1	MPa	Pre-peak hardening	6270	32351	977	(13)
h_2	MPa	Post-peak softening	5030	14827	648	(13)
$\bar{\epsilon}_p$	-	Peak plastic strain	0.027	0.009	0.045	(13)
f	-	Smooth factor	0.3	0.3	0.3	(13)
α_p	-	Pressure sensitivity	0	0	0	(10)
m	-	Rate sensitivity	0.66	0.80	1	(10)&(11)
$\bar{\epsilon}_0$	1/s	Rate sensitivity	329	3.55e+11	6.24e+6	(10)
A	K/MPa	Rate sensitivity	115	104	265	(10)
Network (Rubber effect)						
C^R	MPa	Rubbery modulus	-	-	1.3	(24)&(25)
N	-	number of rigid links	-	-	4	(24)&(25)
Crystalline						
E_c	MPa	Apparent modulus	210	163	26	(-)
ν_c	-	Poisson's ratio	0.39	0.39	0.32	(-)
$\sigma_{c,y0}$	MPa	Initial yield stress	22	19	2.3	(-)

Table A.2

Strain hardening data for the crystalline component.

Nylon 101		PA6		LDPE	
ϵ_B^p (%)	σ_{yt}, σ_{yc} (MPa)	ϵ_B^p (%)	σ_{yt}, σ_{yc} (MPa)	ϵ_B^p (%)	σ_{yt}, σ_{yc} (MPa)
0.0	22.0	0.0	19.0	0.0	2.30
1.8	27.7	0.3	20.9	0.2	2.74
4.4	32.8	0.8	23.4	0.5	3.51
7.7	36.4	1.0	23.9	1.0	4.12
11.5	38.8	1.3	25	1.6	4.57
15.7	40.4	1.9	26.5	3.1	5.19
20.3	41.5	2.6	27.9	4.9	5.60
24.9	42.1	3.1	28.7	6.5	5.80
29.7	42.6	4.1	30.3	8.5	5.94
34.5	43.1	4.9	31.5	9.3	5.98
39.2	43.7	5.4	32.4	10.2	6.00
43.9	44.3	5.6	32.8	10.7	6.01
48.5	45.1	6.0	33.8	13.1	6.02

B. Activation of crystalline phase

The calibration of the characteristic time t_c was performed on a SE (side length of 1 mm) thermomechanical analysis. In this Section, the experimental data of nylon 101 at temperature 22°C was used. Firstly, the contribution of the amorphous phase has to be characterized and validated (see Fig. B.1) following the procedure in Appendix A. Secondly, the following are two needed steps to determine the activation and disclosure of the contribution of crystalline phase:

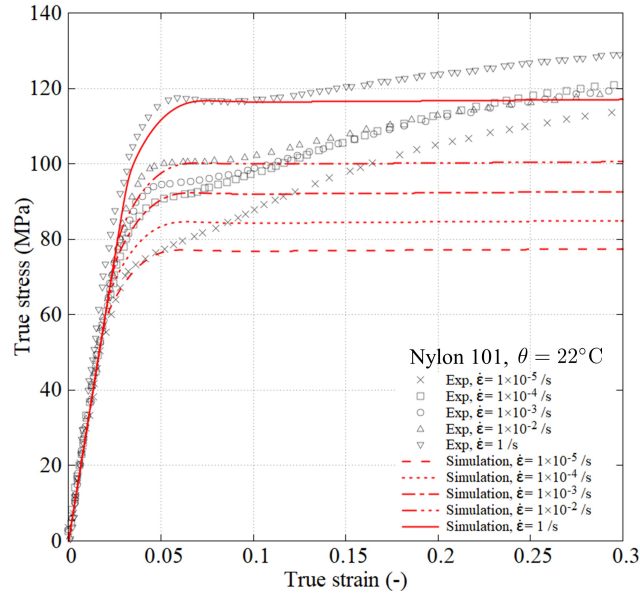


Figure B.1: The validation of rate- and temperature-dependent amorphous contribution.

1. **Activation:** Activate the crystalline rheological component when the first yield occurs. The $\sigma_{y,I}$ can be determined by: (a) finding directly the local maximum, if it exists, in the stress-strain curve or (b) verifying if the equivalent plastic strain rate $\dot{\epsilon}_p$ equals the corresponding applied strain rate $\dot{\epsilon}$ (see Fig. B.2).
2. **Disclosure:** The characteristic time t_c is further determined by fitting the required time period passing from the $\sigma_{y,I}$ to the one when the apparent elastic segment in stress-strain curves is observed (see Fig. B.3). The contribution of crystalline phase is then disclosed with a distinct "small hump" at high strain rate.

Fig. B.1 shows the stress-strain curves generated only by the amorphous contribution. The calibration was done following the third step in Appendix A. The $\sigma_{y,I}$ of the prediction distributes evenly according to the magnitude of applied strain rate. The yield stress increases as the applied strain rate increases. In this procedure it is assumed that the amorphous region achieves the saturated state without strain softening once the $\sigma_{y,I}$ is reached.

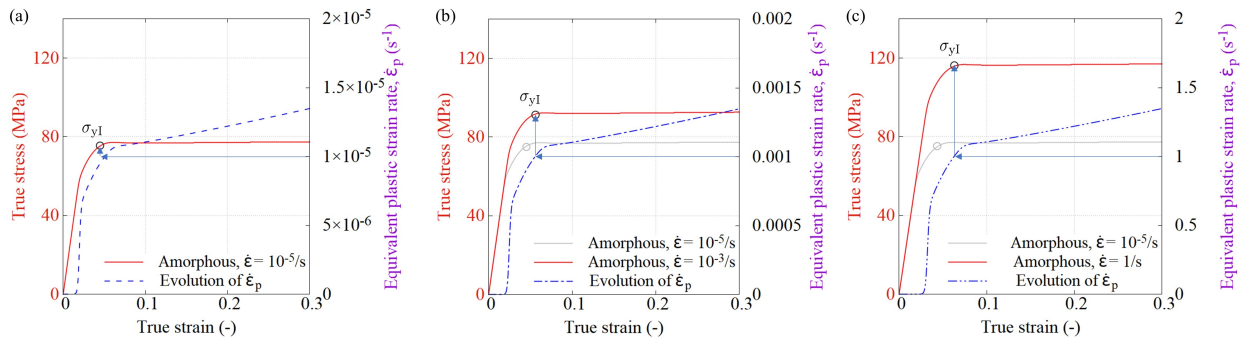


Figure B.2: Internal equivalent plastic strain rates in amorphous phase and the corresponding $\sigma_{y,I}$ at different strain rates: (a) $1 \times 10^{-5} \text{ s}^{-1}$, (b) $1 \times 10^{-3} \text{ s}^{-1}$, and (c) 1 s^{-1} .

Fig. B.2 shows the evolution of the equivalent plastic strain rate (dash lines) at three strain rates: $1 \times 10^{-5} \text{ s}^{-1}$, $1 \times 10^{-3} \text{ s}^{-1}$, and 1 s^{-1} . The stress-strain curve at strain rate $1 \times 10^{-5} \text{ s}^{-1}$ is superposed in all plots. It shows that the first yield stress can be determined as the equivalent plastic strain equals to the applied strain. A migration of first yield to the right can be seen at higher strain rates, in accordance with the experimental observation. The crystalline

Table C.1

Visco-elastic properties of the three Maxwell elements for two study cases.

Case	1			2		
k	1	2	3	1	2	3
G (MPa)	250	500	1000	500	1000	1500
t_R (s)	100	10	1	100	10	1
η (MPa s)	25000	5000	1000	50000	10000	1500

model is activated at this point and the time t_0 is recorded. The underlying crystalline contribution is then disclosed once $t = t_0 + t_c$ (see Fig. B.3).

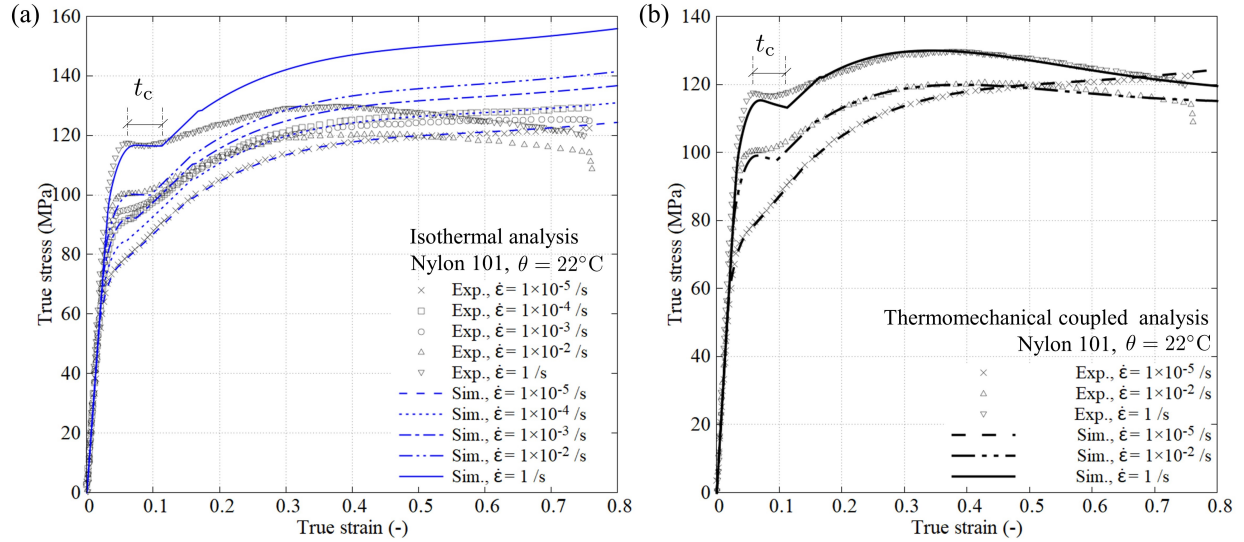


Figure B.3: Comparison between experimental results and the prediction of nylon 101 using SE with (a) isothermal analysis and (b) fully thermomechanical coupled analysis.

Fig. B.3 shows the true stress-strain curves from the predictions under isothermal and non-isothermal conditions. As the strain rate increases from $1 \times 10^{-5} \text{ s}^{-1}$ to 1 s^{-1} , the shape of the macroscopic response conforms well with the prediction of the proposed double yield model. The "small humps" after the first yield in the true stress-strain curves were also quantitatively predicted. The strain required for the establishment of equilibrium between amorphous and crystalline phases increases when the strain rate increases. The contribution of crystalline phase takes place at 12 % strain under 1 s^{-1} , compared to 9 % at $1 \times 10^{-2} \text{ s}^{-1}$.

Fig. B.3(a) implies that the experimental stress-strain curves with downwards trend experience the thermal softening effect. Garcia-Gonzalez *et al.* [2] illustrated the thermal softening effect by representing the isothermal and adiabatic intermolecular resistances. The temperature increase due to the self-heating can hardly reach the crystallization temperature. This confirms that the amorphous intermolecular resistance A is affected directly by the thermal softening rather than the crystalline interlamellar resistance B . Fig. B.3(b) shows three representative thermomechanical behaviours namely isothermal ($\dot{\epsilon} = 1 \times 10^{-5} \text{ s}^{-1}$), coupled ($\dot{\epsilon} = 1 \times 10^{-3} \text{ s}^{-1}$) and nearly adiabatic ($\dot{\epsilon} = 1 \text{ s}^{-1}$) conditions. The parametric study has shown that the prediction can be brought downwards decreasing h , which is equivalent to increase the temperature (see Appendix E). The non-isothermal predictions have a satisfactory agreement compared to the experimental results.

C. Incorporating of the viscoelastic response

The aim of this section is to introduce the viscoelastic response which can be separately identified effortlessly. A parametric study of the implemented viscoelastic response was also performed with two study cases.

Fig. 5 presents the model response including a series of viscoelastic elements connected to the linear elastic component. Each viscoelastic component corresponds to a Maxwell element consisting of an elastic spring and a linear dashpot. In order to decouple the viscoelastic response from the other nonlinear features, total stress σ_A obtained from the linear spring and the Maxwell branches $\sum_{i=1}^{N_{ve}} \sigma_A^{ve,i}$ is passed into the viscoplastic dashpot element as a driving stress (see Eq. (7)). Each linear viscoelastic response is given by $\sigma_A^{ve,i} = \xi \dot{\epsilon}$ with the viscosity $\xi = G t_R$, where G is the shear modulus and t_R the relaxation time. Constant parameters were assumed and three Maxwell elements were chosen for this illustrative study case (see Table C.1). Readers are referred to the implementation of the equivalent kinematic finite strain framework (see details in Ref. [78]). The rate of deformation for a single viscoelastic element is given as follows

$$\mathbf{D} = \mathbf{D}_d + \mathbf{D}_h = \dot{\epsilon}_d^{eq} \mathbf{N}_d + \dot{\epsilon}_h^{eq} \mathbf{N}_h = \dot{\epsilon}_d^{eq} \frac{\boldsymbol{\sigma}'}{\sqrt{2}\sigma^{eq}} + \dot{\epsilon}_h^{eq} \frac{p}{\sqrt{2}\sigma^{eq}} \mathbf{I}, \quad (\text{C.1})$$

where $\dot{\epsilon}_d^{eq}$ and $\dot{\epsilon}_h^{eq}$ stand for the deviatoric and hydrostatic equivalent visco strain rates, p is the hydrostatic pressure and \mathbf{I} is the second order identity tensor.

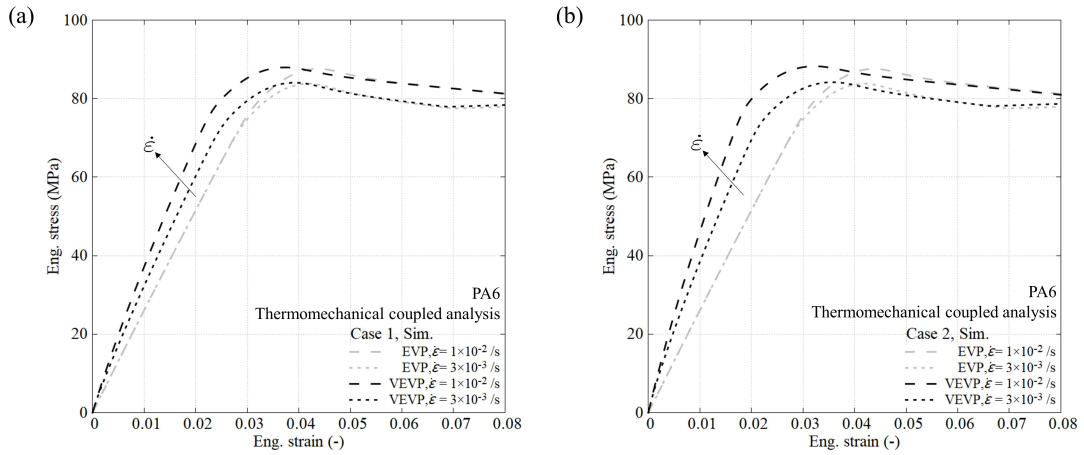


Figure C.1: Comparison of simulated stress-strain curves with two parameter sets of viscoelastic response

Fig. C.1 presents the simulated results based on the dog-bone test on PA6 (see Section 8.2) assuming the hypothetical values of the viscoelastic parameters from Table C.1. These values were deliberately chosen to cover a sufficiently wide range of the relaxation time and elasticity. The elasto-viscoplastic result, grey lines, are plotted as a guidance in Fig. C.1. Two strain rates, 0.01 s^{-1} and 0.003 s^{-1} , are examined. The results with viscoelastic response show that first yield move leftwards but maintain the same level of stress, and following the strain softening segment regardless of the adopted viscoelastic parameter set. The modulus becomes rate-dependent and increases as the applied strain rate increases. The viscoelastic parameter set with larger shear moduli for the Maxwell elements provides a higher instantaneous modulus. The advantages of this arrangement are clear: (a) it does not affect the contribution of the amorphous and crystalline phases, and (b) the parameter identification for viscoelastic response can be separated from the aforementioned calibration tests using a Dynamic Mechanical Analyser (DMA).

D. Parameter sensitivity analyses of the hyperelastic response

The rubbery effect of the network resistance C contribution on the proposed double yield model was examined (see Fig. D.1). It was studied with the same parameter set from nylon 101 but adding the rubbery effect (see Table A.1). For the sake of simplicity, only a three-chain model is illustrated ($\kappa = 0$). Two parameters, the rubbery modulus C^R and the average number of links N , were studied at the temperature 22°C and under two strain rates namely $\dot{\epsilon} = 1 \times 10^{-5} \text{ s}^{-1}$ and $\dot{\epsilon} = 1 \times 10^{-2} \text{ s}^{-1}$. The rubbery effect becomes visible under large strain range by decreasing the magnitude of N or increasing C^R .

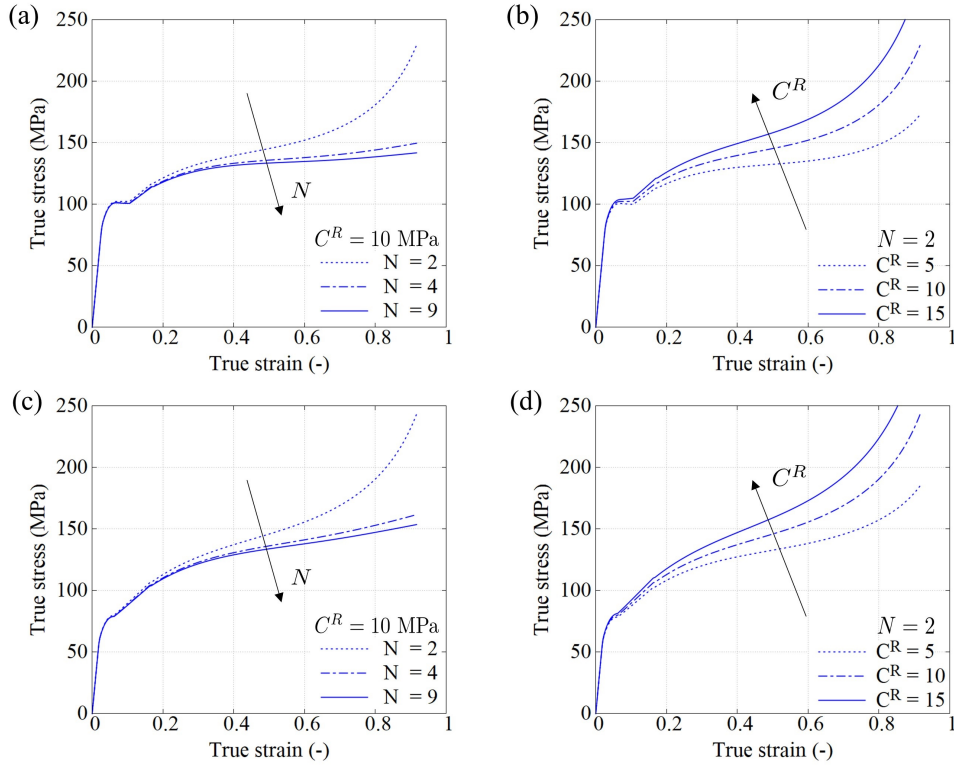


Figure D.1: Parameter sensitivity analyses on rubbery effect in double yield model at strain rate (a and b) $1 \times 10^{-2} \text{ s}^{-1}$ and (c and d) $1 \times 10^{-5} \text{ s}^{-1}$.

E. Effect of thermal parameters

To enrich the flexibility of the proposed model, a constant, inelastic heat fraction η , can be introduced to generate a volumetric heat flux source term partially from the energy dissipation. Unlike fluid-like materials, the stored energy was a constant fraction of plastic work so that the full heat conversion is unlikely to occur in solid materials (refer to Ref. [91]). Meanwhile, η is used to mediate the underestimation of heat source associated with deformations, for instance, the assumption of neglecting some terms while deriving Eq. (37). The η is determined by using adiabatic condition. Assuming constant thermal properties, the heat equation is extended as follows

$$\rho c_p \frac{\partial \theta}{\partial t} = \eta (\boldsymbol{\sigma}_A : \mathbf{F}_A^e \mathbf{L}_A^p (\mathbf{F}_A^e)^{-1} + \boldsymbol{\sigma}_B : \mathbf{F}_B^e \mathbf{L}_B^p (\mathbf{F}_B^e)^{-1}) + \nabla \cdot \left(k \frac{\partial \theta}{\partial \mathbf{x}} \right). \quad (\text{E.1})$$

The convection coefficient h can be experimentally obtained or estimated using a model assuming natural convection on a vertical surface. In practice, h can be obtained by fitting the stress-strain curves at a moderate strain rate in the thermal coupled regime. Furthermore, the thermal softening is incorporated by the temperature-dependent modulus $E_A(\theta)$ via a material constant β .

Fig. E.2 shows the effects of parameters η , β and h using a SE analysis. Nylon 101 at a reference temperature $\theta = 22^\circ\text{C}$ and $\dot{\epsilon} = 1 \times 10^{-2} \text{ s}^{-1}$ was used. The solid line represents the response using the calibrated parameters (see Appendix A). It can be seen that the true stress-strain curve is brought downwards by decreasing h , or increasing η and β .

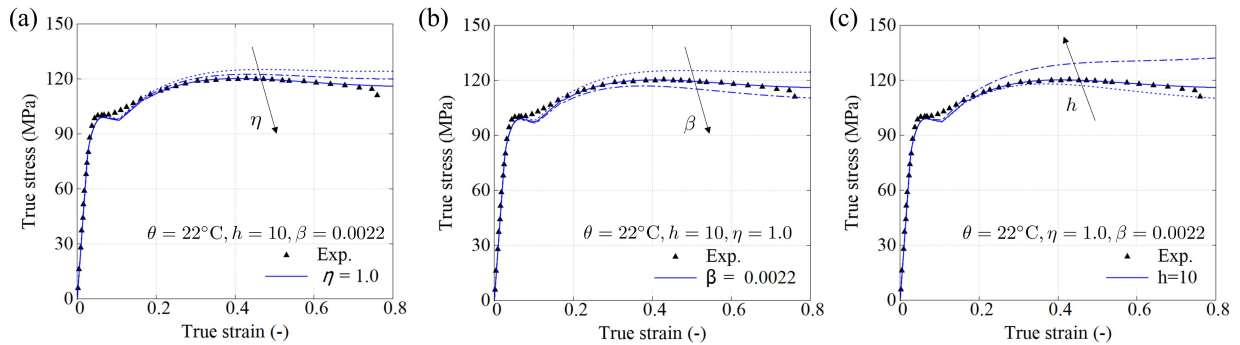


Figure E.2: Variation of the true stress-true strain curves of nylon 101 at strain rate of $1 \times 10^{-2} \text{ s}^{-1}$ affected by (a) inelastic heat fraction η , (b) temperature-dependent β and (c) convection coefficient h .

References

- [1] V. Srivastava, S. A. Chester, N. M. Ames, and L. Anand. A thermo-mechanically-coupled large-deformation theory for amorphous polymers in a temperature range which spans their glass transition. *Int. J. Plast.*, 26(8):1138–1182, 2010. doi: 10.1016/j.ijplas.2010.01.004.
- [2] D. Garcia-Gonzalez, R. Zaera, and A. Arias. A hyperelastic-thermoviscoplastic constitutive model for semi-crystalline polymers: Application to PEEK under dynamic loading conditions. *Int. J. Plast.*, 88:27–52, 2017. doi: 10.1016/j.ijplas.2016.09.011.
- [3] E. Parodi, G. W. M. Peters, and L. E. Govaert. Prediction of plasticity-controlled failure in polyamide 6: Influence of temperature and relative humidity. *J. Appl. Polym. Sci.*, 135(11):45942, 2018. doi: 10.1002/app.45942.
- [4] J. Johnsen, A. H. Clausen, F. Grytten, A. Benallal, and O. S. Hopperstad. A thermo-elasto-viscoplastic constitutive model for polymers. *J. Mech. Phys. Solids*, 124:681–701, 2019. doi: 10.1016/j.jmps.2018.11.018.
- [5] A. Krairi, I. Doghri, J. Schalnath, G. Robert, and W. Van Paeppegem. Thermo-mechanical coupling of a viscoelastic-viscoplastic model for thermoplastic polymers: Thermodynamical derivation and experimental assessment. *Int. J. Plast.*, 115:154–177, 2019. doi: 10.1016/j.ijplas.2018.11.016.
- [6] S. Felder, H. Holthusen, S. Hesseler, F. Pohlkemper, T. Gries, J.-W. Simon, and S. Reese. Incorporating crystallinity distributions into a thermo-mechanically coupled constitutive model for semi-crystalline polymers. *Int. J. Plast.*, 135:102751, 2020. doi: 10.1016/j.ijplas.2020.102751.
- [7] F. Detrez, S. Cantournet, and R. Séguela. Plasticity/damage coupling in semi-crystalline polymers prior to yielding: Micromechanisms and damage law identification. *Polymer*, 52(9):1998–2008, 2011. doi: 10.1016/j.polymer.2011.03.012.
- [8] S. Humbert, O. Lame, R. Séguela, and G. Vigier. A re-examination of the elastic modulus dependence on crystallinity in semi-crystalline polymers. *Polymer*, 52(21):4899–4909, 2011. doi: 10.1016/j.polymer.2011.07.060.
- [9] B. Xiong, O. Lame, J.M. Chenal, C. Rochas, R. Séguela, and G. Vigier. In-situ SAXS study and modeling of the cavitation/crystal-shear competition in semi-crystalline polymers: Influence of temperature and microstructure in polyethylene. *Polymer*, 54(20):5408–5418, 2013. doi: 10.1016/j.polymer.2013.07.055.
- [10] V. Ferreiro and G. Coulon. Shear banding in strained semicrystalline polyamide 6 films as revealed by atomic force microscopy: role of the amorphous phase. *J. Polym. Sci. B Polym. Phys.*, 42(4):687–701, 2004. doi: 10.1002/polb.10731.
- [11] C. Thomas, R. Seguela, F. Detrez, V. Miri, and C. Vanmansart. Plastic deformation of spherulitic semi-crystalline polymers: An in situ AFM study of polybutene under tensile drawing. *Polymer*, 50(15):3714–3723, 2009. doi: 10.1016/j.polymer.2009.06.023.
- [12] A. S. Khan and B. Farrokh. Thermo-mechanical response of nylon 101 under uniaxial and multi-axial loadings: Part I, Experimental results over wide ranges of temperatures and strain rates. *Int. J. Plast.*, 22(8):1506–1529, 2006. doi: 10.1016/j.ijplas.2005.10.001.
- [13] H. Luo, Z. Fu, B. Jing, J. Shi, X. Zou, and W. Dai. Tensile behaviors of polyamide 6/UHLE blends. *J. Mater. Sci.*, 44(14):3694–3701, 2009. doi: 10.1007/s10853-009-3494-8.
- [14] A. Benaarbia, A. Chrysochoos, and G. Robert. Influence of relative humidity and loading frequency on the PA6.6 cyclic thermomechanical behavior: Part I. mechanical and thermal aspects. *Polym. Test.*, 40:290–298, 2014. doi: 10.1016/j.polymertesting.2014.09.019.
- [15] L. Laiarinandrasana, N. Selles, O. Klinkova, T. F. Morgeneyer, H. Proudhon, and L. Helfen. Structural versus microstructural evolution of semi-crystalline polymers during necking under tension: Influence of the skin-core effects, the relative humidity and the strain rate. *Polym. Test.*, 55:297–309, 2016. doi: 10.1016/j.polymertesting.2016.09.012.
- [16] E. Parodi. *Structure properties relations for polyamide 6*. PhD thesis, Department of Mechanical Engineering, 2017. Proefschrift.
- [17] P Venkatraman, A. M. Gohn, A. M. Rhoades, and E. J. Foster. Developing high performance PA 11/cellulose nanocomposites for industrial-scale melt processing. *Compos. B. Eng.*, 174:106988, 2019. doi: 10.1016/j.compositesb.2019.106988.
- [18] J. Zhang. Study of poly(trimethylene terephthalate) as an engineering thermoplastics material. *J. Appl. Polym. Sci.*, 91(3):1657–1666, 2004. doi: 10.1002/app.13322.
- [19] N. W. Brooks, R. A. Duckett, and I. M. Ward. Investigation into double yield points in polyethylene. *Polymer*, 33(9):1872–1880, 1992. doi: 10.1016/0032-3861(92)90486-G.
- [20] A. Sedighiamiri, L. E. Govaert, and J. A. W. van Dommelen. Micromechanical modeling of the deformation kinetics of semicrystalline polymers. *J. Polym. Sci. B Polym. Phys.*, 49(18):1297–1310, 2011. doi: 10.1002/polb.22297.

- [21] M. A. AlMaadeed, Z. Nógellová, M Mičušík, I. Novák, and I. Krupa. Mechanical, sorption and adhesive properties of composites based on low density polyethylene filled with date palm wood powder. *Mater. Des.*, 53:29–37, 2014. doi: 10.1016/j.matdes.2013.05.093. 820
- [22] J. L. Jordan, D. T. Casem, J. M. Bradley, A. K. Dwivedi, E. N. Brown, and C. W. Jordan. Mechanical properties of low density polyethylene. *J. Dyn. Behav. Mater.*, 2(4):411–420, 2016. doi: 10.1007/s40870-016-0076-0. 822
- [23] A. Rozanski and A. Galeski. Plastic yielding of semicrystalline polymers affected by amorphous phase. *Int. J. Plast.*, 41:14–29, 2013. doi: 10.1016/j.ijplas.2012.07.008. 824
- [24] A. Krajenta and A. Rozanski. Physical state of the amorphous phase of polypropylene-influence on thermo-mechanical properties. *Polymer*, 70:127–138, 2015. doi: 10.1016/j.polymer.2015.06.020. 826
- [25] Z. Bartzczak and A. Galeski. Plasticity of semicrystalline polymers. *Macromol. Symp.*, 294(1):67–90, 2010. doi: 10.1002/masy.201050807. 828
- [26] A. R. Plaza, E. Ramos, A. Manzur, R. Olayo, and A. Escobar. Double yield points in triblend of LDPE, LLDPE and EPDM. *J. Mater. Sci.*, 32(2):549–554, 1997. doi: 10.1023/A:1018554828007. 829
- [27] Y. Zhang, P.-Y. Ben Jar, S. Xue, and L. Li. Quantification of strain-induced damage in semi-crystalline polymers: a review. *J. Mater. Sci.*, 54(1):62–82, 2019. doi: 10.1007/s10853-018-2859-2. 831
- [28] C. G’sell and A. Dahoun. Evolution of microstructure in semi-crystalline polymers under large plastic deformation. *Mater. Sci. Eng. A*, 175(1):183–199, 1994. doi: 10.1016/0921-5093(94)91058-8. 833
- [29] E. Parodi, G. W. M. Peters, and L. E. Govaert. Structure–properties relations for polyamide 6, part 1: influence of the thermal history during compression moulding on deformation and failure kinetics. *Polymers*, 10(7), 2018. doi: 10.3390/polym10070710. 835
- [30] K. Nitta and M. Kuriyagawa. Application of catastrophe theory to neck initiation of metallocene-catalyzed high-density polyethylene. *Polym. J.*, 44:245–251, 2012. doi: 10.1038/pj.2011.119. 837
- [31] B. Farrokh and AS. Khan. A strain rate dependent yield criterion for isotropic polymers: Low to high rates of loading. *Eur. J. Mech. A/Solids*, 29(2):274–282, 2010. doi: 10.1016/j.euromechsol.2009.08.004. 839
- [32] K. Hachour, F. Zaïri, M. Naït-Abdelaziz, J.M. Gloaguen, M. Aberkane, and J.M. Lefebvre. Experiments and modeling of high-crystalline polyethylene yielding under different stress states. *Int. J. Plast.*, 54:1–18, 2014. doi: 10.1016/j.ijplas.2013.06.004. 841
- [33] M. Polířská, A. Rozanski, A. Galeski, and J. Bojda. The modulus of the amorphous phase of semicrystalline polymers. *Macromolecules*, 54(19):9113–9123, 2021. doi: 10.1021/acs.macromol.1c01576. 843
- [34] D. Lai, I. Yakimets, and M. Guigon. A non-linear viscoelastic model developed for semi-crystalline polymer deformed at small strains with loading and unloading paths. *Mater. Sci. Eng. A*, 405(1):266–271, 2005. doi: 10.1016/j.msea.2005.06.011. 845
- [35] G. Ayoub, F. Zaïri, M. Naït-Abdelaziz, and J.M. Gloaguen. Modelling large deformation behaviour under loading–unloading of semicrystalline polymers: Application to a high density polyethylene. *Int. J. Plast.*, 26(3):329–347, 2010. doi: 10.1016/j.ijplas.2009.07.005. 847
- [36] O. U. Colak. Modeling deformation behavior of polymers with viscoplasticity theory based on overstress. *Int. J. Plast.*, 21(1):145–160, 2005. doi: 10.1016/j.ijplas.2004.04.004. 849
- [37] N. Dusunceli and O. U. Colak. Modelling effects of degree of crystallinity on mechanical behavior of semicrystalline polymers. *Int. J. Plast.*, 24(7):1224–1242, 2008. doi: 10.1016/j.ijplas.2007.09.003. 851
- [38] F. Khan and C. Yeakle. Experimental investigation and modeling of non-monotonic creep behavior in polymers. *Int. J. Plast.*, 27(4):512–521, 2011. doi: 10.1016/j.ijplas.2010.06.007. 853
- [39] F. Khan, C. Yeakle, and S. Goma. Characterization of the mechanical properties of a new grade of ultra high molecular weight polyethylene and modeling with the viscoplasticity based on overstress. *J. Mech. Behav. Biomed. Mater.*, 6:174–180, 2012. doi: 10.1016/j.jmbbm.2011.10.009. 855
- [40] A. D. Drozdov and J. C. Christiansen. Cyclic viscoplasticity of high-density polyethylene: Experiments and modeling. *Comput. Mater. Sci.*, 39(2):465–480, 2007. doi: 10.1016/j.commatsci.2006.07.014. 858
- [41] A. Khan and H. Zhang. Finite deformation of a polymer: experiments and modeling. *Int. J. Plast.*, 17(9):1167–1188, 2001. doi: 10.1016/S0749-6419(00)00073-5. 860
- [42] R. Balieu, F. Lauro, B. Bennani, R. Delille, T. Matsumoto, and E. Mottola. A fully coupled elastoviscoplastic damage model at finite strains for mineral filled semi-crystalline polymer. *Int. J. Plast.*, 51:241–270, 2013. doi: 10.1016/j.ijplas.2013.05.002. 862
- [43] R. Balieu, F. Lauro, B. Bennani, G. Haugou, F. Chaari, T. Matsumoto, and E. Mottola. Damage at high strain rates in semi-crystalline polymers. *Int. J. Impact Eng.*, 76:1–8, February 2015. doi: 10.1016/j.ijimpeng.2014.08.013. 863
- [44] E. Ghorbel. A viscoplastic constitutive model for polymeric materials. *Int. J. Plast.*, 24(11):2032–2058, 2008. doi: 10.1016/j.ijplas.2008.01.003. 866
- [45] B. Miled, I. Doghri, and L. Delannay. Coupled viscoelastic–viscoplastic modeling of homogeneous and isotropic polymers: Numerical algorithm and analytical solutions. *Comput. Methods Appl. Mech. Eng.*, 200(47):3381–3394, 2011. doi: 10.1016/j.cma.2011.08.015. 868
- [46] C. Yu, G. Kang, and K. Chen. A hygro-thermo-mechanical coupled cyclic constitutive model for polymers with considering glass transition. *Int. J. Plast.*, 89:29–65, 2017. doi: 10.1016/j.ijplas.2016.11.001. 870
- [47] B. J. Lee, D. M. Parks, and S. Ahzi. Micromechanical modeling of large plastic deformation and texture evolution in semi-crystalline polymers. *J. Mech. Phys. Solids*, 41(10):1651–1687, 1993. doi: 10.1016/0022-5096(93)90018-B. 872
- [48] B. J. Lee, A. S. Argon, D. M. Parks, S. Ahzi, and Z. Bartzczak. Simulation of large strain plastic deformation and texture evolution in high density polyethylene. *Polymer*, 34(17):3555–3575, 1993. doi: 10.1016/0032-3861(93)90039-D. 874
- [49] S. Nikolov and I. Doghri. A micro/macro constitutive model for the small-deformation behavior of polyethylene. *Polymer*, 41(5):1883–1891, 2000. doi: 10.1016/S0032-3861(99)00330-4. 876
- [50] S. Nikolov, I. Doghri, O. Pierard, L. Zealouk, and A. Goldberg. Multi-scale constitutive modeling of the small deformations of semi-crystalline polymers. *J. Mech. Phys. Solids*, 50(11):2275–2302, 2002. doi: 10.1016/S0022-5096(02)00036-4. 878
- [51] J. A. W. van Dommelen, D. M. Parks, M. C. Boyce, W. A. M. Brekelmans, and F. P. T. Baaijens. Micromechanical modeling of the elastoviscoplastic behavior of semi-crystalline polymers. *J. Mech. Phys. Solids*, 51(3):519–541, 2003. doi: 10.1016/S0022-5096(02)00063-7. 880

- [52] F. Bédoui, J. Diani, G. Régnier, and W. Seiler. Micromechanical modeling of isotropic elastic behavior of semicrystalline polymers. *Acta Mater.*, 54(6):1513–1523, 2006. doi: 10.1016/j.actamat.2005.11.028. 882
- [53] A. Shojaei and G. Li. Viscoplasticity analysis of semicrystalline polymers: A multiscale approach within micromechanics framework. *Int. J. Plast.*, 42:31–49, 2013. doi: 10.1016/j.ijplas.2012.09.014. 883
- [54] M. Uchida and N. Tada. Micro-, meso- to macroscopic modeling of deformation behavior of semi-crystalline polymer. *Int. J. Plast.*, 49: 164–184, 2013. doi: 10.1016/j.ijplas.2013.03.007. 884
- [55] G.Z. Voyiadjis, A. Shojaei, and N. Mozaffari. Strain gradient plasticity for amorphous and crystalline polymers with application to micro- and nano-scale deformation analysis. *Polymer*, 55(16):4182–4198, 2014. doi: 10.1016/j.polymer.2014.06.015. 885
- [56] S. Ahzi, A. Makradi, R. V. Gregory, and D. D. Edie. Modeling of deformation behavior and strain-induced crystallization in poly(ethylene terephthalate) above the glass transition temperature. *Mech. Mater.*, 35(12):1139–1148, 2003. doi: 10.1016/S0167-6636(03)00004-8. 886
- [57] M. C. Boyce, S. Socrate, and P. G. Llana. Constitutive model for the finite deformation stress–strain behavior of poly(ethylene terephthalate) above the glass transition. *Polymer*, 41(6):2183–2201, 2000. doi: 10.1016/S0032-3861(99)00406-1. 887
- [58] A. Makradi, S. Ahzi, R. V. Gregory, and D. D. Edie. A two-phase self-consistent model for the deformation and phase transformation behavior of polymers above the glass transition temperature: application to PET. *Int. J. Plast.*, 21(4):741–758, 2005. doi: 10.1016/j.ijplas.2004.04.012. 888
- [59] G. Ayoub, F. Zaïri, C. Fréderix, J. M. Gloaguen, M. Naït-Abdelaziz, R. Seguela, and J. M. Lefebvre. Effects of crystal content on the mechanical behaviour of polyethylene under finite strains: Experiments and constitutive modelling. *Int. J. Plast.*, 27(4):492–511, 2011. doi: 10.1016/j.ijplas.2010.07.005. 889
- [60] H. Abdul-Hameed, T. Messenger, G. Ayoub, F. Zaïri, M. Naït-Abdelaziz, Z. Qu, and F. Zaïri. A two-phase hyperelastic-viscoplastic constitutive model for semi-crystalline polymers: Application to polyethylene materials with a variable range of crystal fractions. *J. Mech. Behav. Biomed. Mater.*, 37:323–332, 2014. ISSN 17516161. doi: 10.1016/j.jmbbm.2014.04.016. 890
- [61] H. A. Cayzac, K. Saï, and L. Lailarinandrasana. Damage based constitutive relationships in semi-crystalline polymer by using multi-mechanisms model. *Int. J. Plast.*, 51:47–64, 2013. doi: 10.1016/j.ijplas.2013.06.008. 891
- [62] C.M. Popa, R. Fleischhauer, K. Schneider, and M. Kaliske. Formulation and implementation of a constitutive model for semicrystalline polymers. *Int. J. Plast.*, 61:128–156, October 2014. ISSN 07496419. doi: 10.1016/j.ijplas.2014.05.010. 892
- [63] G. Ayoub, A.K. Rodriguez, B. Mansoor, and X. Colin. Modeling the visco-hyperelastic–viscoplastic behavior of photodegraded semi-crystalline low-density polyethylene films. *Int. J. Solids Struct.*, 204-205:187–198, 2020. doi: 10.1016/j.ijsolstr.2020.08.025. 893
- [64] A. Maurel-Pantel, E. Baquet, J. L. Bikard, J. L. Bouvard, and N. Billon. A thermo-mechanical large deformation constitutive model for polymers based on material network description: Application to a semi-crystalline polyamide 66. *Int. J. Plast.*, 67:102–126, 2015. doi: 10.1016/j.ijplas.2014.10.004. 894
- [65] N. Billon. New constitutive modeling for time-dependent mechanical behavior of polymers close to glass transition: Fundamentals and experimental validation. *J. Appl. Polym. Sci.*, 125(6):4390–4401, 2012. doi: 10.1002/app.36598. 895
- [66] E. M. Arruda, M. C. Boyce, and R. Jayachandran. Effects of strain rate, temperature and thermomechanical coupling on the finite strain deformation of glassy polymers. *Mech. Mater.*, 19(2-3):193–212, 1995. doi: 10.1016/0167-6636(94)00034-E. 896
- [67] Lallit Anand, Nicoli M. Ames, Vikas Srivastava, and Shawn A. Chester. A thermo-mechanically coupled theory for large deformations of amorphous polymers. Part I: Formulation. *Int. J. Plast.*, 25(8):1474–1494, 2009. doi: 10.1016/j.ijplas.2008.11.004. 897
- [68] Nicoli M. Ames, Vikas Srivastava, Shawn A. Chester, and Lallit Anand. A thermo-mechanically coupled theory for large deformations of amorphous polymers. Part II: Applications. *Int. J. Plast.*, 25(8):1495–1539, 2009. doi: 10.1016/j.ijplas.2008.11.005. 898
- [69] R.K. Jena, S.A. Chester, V. Srivastava, C.Y. Yue, L. Anand, and Y.C. Lam. Large-strain thermo-mechanical behavior of cyclic olefin copolymers: Application to hot embossing and thermal bonding for the fabrication of microfluidic devices. *Sens. Actuators B Chem.*, 155 (1):93–105, 2011. doi: 10.1016/j.snb.2010.11.031. 899
- [70] J.L. Bouvard, D.K. Francis, M.A. Tschopp, E.B. Marin, D.J. Bammann, and M.F. Horstemeyer. An internal state variable material model for predicting the time, thermomechanical, and stress state dependence of amorphous glassy polymers under large deformation. *Int. J. Plast.*, 42: 168–193, 2013. doi: 10.1016/j.ijplas.2012.10.005. 900
- [71] A. Maurel-Pantel, E. Baquet, J. Bikard, J. L. Bouvard, and N. Billon. A thermo-mechanical large deformation constitutive model for polymers based on material network description: application to a semi-crystalline polyamide 66. *Int. J. Plast.*, 67:102–126, 2015. doi: 10.1016/j.ijplas.2014.10.004. 901
- [72] K. Chen, G. Kang, F. Lu, J. Chen, and H. Jiang. Effect of relative humidity on uniaxial cyclic softening/hardening and intrinsic heat generation of polyamide-6 polymer. *Polym. Test.*, 56:19–28, 2016. doi: 10.1016/j.polymertesting.2016.09.020. 902
- [73] F. Shen, G. Kang, Y. C. Lam, Y. Liu, and K. Zhou. Thermo-elastic-viscoplastic-damage model for self-heating and mechanical behavior of thermoplastic polymers. *Int. J. Plast.*, 121:227–243, 2019. doi: 10.1016/j.ijplas.2019.06.003. 903
- [74] X. Poulain, A.A. Benzerga, and R.K. Goldberg. Finite-strain elasto-viscoplastic behavior of an epoxy resin: Experiments and modeling in the glassy regime. *Int. J. Plast.*, 62:138–161, 2014. doi: 10.1016/j.ijplas.2014.07.002. 904
- [75] A. S. Argon. A theory for the low-temperature plastic deformation of glassy polymers. *Philos. Mag.*, 28(4):839–865, 1973. doi: 10.1080/14786437308220987. 905
- [76] M. Donnay, M. Ponçot, J. Tinnes, T. Schenk, O. Ferry, and I. Royaud. In situ study of the tensile deformation micro-mechanisms of semi-crystalline poly(ethylene terephthalate) films using synchrotron radiation X-ray scattering. *Polymer*, 117:268–281, 2017. doi: 10.1016/j.polymer.2017.04.043. 906
- [77] R. N. Haward, G. Thackray, and Theodore Morris Sugden. The use of a mathematical model to describe isothermal stress-strain curves in glassy thermoplastics. *Proceedings of the Royal Society of London. Series A. Mathematical and Physical Sciences*, 302(1471):453–472, 1968. doi: 10.1098/rspa.1968.0029. 907
- [78] F. A. Gilabert. Modelling nonlinear material response of polymer matrices used in fiber-reinforced composites. In W. van Paepegem, editor, *Multi-scale continuum mechanics modelling of fibre-reinforced polymer composites*, Woodhead Publishing Series in Composites Science and Engineering, pages 219–242. Woodhead, 2020. ISBN 9780128189849. 908

- [79] M.C. Boyce, G.G. Weber, and D.M. Parks. On the kinematics of finite strain plasticity. *J. Mech. Phys. Solids*, 37(5):647–665, 1989. doi: 10.1016/0022-5096(89)90033-1. 945
- [80] M. C. Boyce, D. M. Parks, and A. S. Argon. Large inelastic deformation of glassy polymers. part I: rate dependent constitutive model. *Mech. Mater.*, 7(1):15–33, 1988. doi: 10.1016/0167-6636(88)90003-8. 946
- [81] T. A. Tervoort, E. T. J. Klompen, and L. E. Govaert. A multi-mode approach to finite, three-dimensional, nonlinear viscoelastic behavior of polymer glasses. *J. Rheol.*, 40(5):779–797, 1996. doi: 10.1122/1.550755. 947
- [82] E. T. J. Klompen, T. A. P. Engels, L. E. Govaert, and H. E. H. Meijer. Modeling of the postyield response of glassy polymers: influence of thermomechanical history. *Macromolecules*, 38(16):6997–7008, 2005. doi: 10.1021/ma050498v. 948
- [83] L.C.A. van Breemen, E.T.J. Klompen, L.E. Govaert, and H.E.H. Meijer. Extending the egg constitutive model for polymer glasses to multiple relaxation times. *J. Mech. Phys. Solids*, 59(10):2191–2207, 2011. doi: 10.1016/j.jmps.2011.05.001. 949
- [84] H.X. Li and C.P. Buckley. Necking in glassy polymers: effects of intrinsic anisotropy and structural evolution kinetics in their viscoplastic flow. *Int. J. Plast.*, 26(12):1726–1745, 2010. doi: 10.1016/j.ijplas.2010.02.004. 950
- [85] K. A. Chowdhury, R. Talreja, and A. A. Benzerga. Effects of manufacturing-induced voids on local failure in polymer-based composites. *J. Eng. Mater. Technol.*, 130(021010), 2008. doi: 10.1115/1.2841529. 951
- [86] V. Laheri, P. Hao, and F.A. Gilabert. Efficient non-iterative modelling of pressure-dependent plasticity using paraboloidal yield criterion. *Int. J. Mech. Sci.*, page 106988, 2021. doi: 10.1016/j.ijmecsci.2021.106988. 952
- [87] E. M. Arruda and M. C. Boyce. Evolution of plastic anisotropy in amorphous polymers during finite straining. *Int. J. Plast.*, 9(6):697–720, 1993. doi: 10.1016/0749-6419(93)90034-N. 953
- [88] P. D. Wu and E. Van Der Giessen. On improved network models for rubber elasticity and their applications to orientation hardening in glassy polymers. *J. Mech. Phys. Solids*, 41(3):427–456, 1993. doi: 10.1016/0022-5096(93)90043-F. 954
- [89] E. Krempl. Models of viscoplasticity some comments on equilibrium (back) stress and drag stress. *Acta Mech.*, 69(1-4):25–42, 1987. doi: 10.1007/BF01175712. 955
- [90] S. Kweon and A. A. Benzerga. Finite element implementation of a macromolecular viscoplastic polymer model: implementation of a macromolecular viscoplastic polymer model. *Int. J. Numer. Meth. Engng*, 94(10):895–919, 2013. doi: 10.1002/nme.4474. 956
- [91] Q. Kan, G. Kang, W. Yan, Y. Zhu, and H. Jiang. A thermo-mechanically coupled cyclic plasticity model at large deformations considering inelastic heat generation. In *Proc. of 13th International Conference on Fracture*, 2013. 957